

## ABSTRACT

Title of thesis:        FABRICATION, CHARACTERIZATION AND APPLICATION  
                                 OF HIGH DENSITY GAS TARGETS FOR INTENSE LASER  
                                 INTERACTION EXPERIMENTS

Yuan Yan Tay, Master of Science, 2019

Thesis directed by : Professor Ki-Yong Kim

Institute for Research in Electronics and Applied Physics

University of Maryland

We report on the generation and characterization of submillimetric Argon gas jets with peak density higher than  $10^{21}$  atoms/cm<sup>3</sup> from capillary nozzles of varying throat diameter in the range of 50-450  $\mu$ m. The use of gas jet targets to generate a suitably dense, reliable, and reproducible interaction medium is particularly important in the broad field of laser-plasma interactions, in areas such as high energy density physics (HEDP), plasma waveguides, electron/ion acceleration and x-ray generation.

Here, it is essential to place those targets in the laser focus with subwavelength accuracy and have control over the gas flow using a sonic or supersonic nozzle to provide the desired interaction density. The use of a sonic or supersonic gas flow provides a Gaussian like or plateau neutral density profile. By changing the gas pressure and temperature, one can change the initial neutral density and by using a combination of gases, one can obtain plasmas with multiple ions species, which is needed to localize electrons injection for innovative laser-plasma accelerator schemes. In this thesis, we present a study of the specific characteristics of gas jets produced by micron-sized nozzles in the context of laser-plasma physics. The study is based on experimental work on gas jets of varying sizes and parameters such as backing pressure and temperature.

The thesis is organized as follows: Chapter 1 examines the motivation for generating such high density gas jets in the context of laser wakefield acceleration and the flow physics of supersonic gas jets. Chapter 2 presents the work in manufacturing the nozzles and characterizing the gas jets produced from the straight capillary nozzles using interferometry methods to measure the density profiles and Rayleigh Scattering to identify clusters in the target. Chapter 3 explores the possible applications of the gas jets in terms of generating gas targets in atmospheric conditions, producing icy filament targets by cooling and demonstrating multi-nozzle arrays.

FABRICATION, CHARACTERIZATION AND APPLICATION OF HIGH DENSITY GAS TARGETS  
FOR INTENSE LASER INTERACTION EXPERIMENTS

by

Yuan Yan Tay

Thesis submitted to the Faculty of the Graduate School of the

University of Maryland, College Park, in partial fulfillment

of the requirements for the degree of

Master of Science

2019

Advisory Committee:

Professor Ki-Yong Kim, Chair

Professor Phillip Sprangle

Professor Antonio Ting

© Copyright by

Yuan Yan Tay

2019

## **Acknowledgments**

First and most importantly, I would like to thank Dr Kim for giving me the opportunity to work in his research group for the past six years. Dr Kim's guidance and patience is the main reason I was able to complete this thesis and I am truly grateful that he put faith in me. Dr Kim accepted me to work on an experiment as an undergraduate student and then allowed me to continue to delve deeper into the research topic as a graduate student. Though not always easy, it was a pleasure working in the research environment he worked so hard to build.

I would like to thank my family, especially my parents in Malaysia who supported my decision to further my studies in the US and encouraged me to challenge myself. My extended family here in the US, including my aunt Sherene's and cousin Charlene's family have also been an incredible support pillar over the years. Many fellow graduate students and friends also helped navigate the challenges along the way, especially Steffi and Tim for proofreading this thesis.

There are many others at the Institute for Research in Electronics and Applied Physics who deserve my gratitude. Postdoctoral researchers including Dr You and Dr Kuk for important discussions on the research topic and undergraduate student Luke who assisted in several experiments helped progress the work.

# Table of Contents

Acknowledgments	ii
Table of Contents	iii
List of Figures	iv
Chapter 1 Introduction	
1.1 Motivation and Outline	1
1.2 Supersonic Gas Jets - Flow Physics	4
1.3 Laser Wakefield Acceleration	5
Chapter 2 Gas Jet Characterization	
2.1 Manufacturing Straight Capillary Nozzles	7
2.2 Experimental Setup	
2.2.1 Mach-Zehnder Interferometer	11
2.2.2 Vacuum Chamber	14
2.2.3 Cooling and Temperature Control	15
2.3 Interferometry Analysis	
2.3.1 Phase Extraction	17
2.3.2 Abel Inversion	21
2.4 Results and Analysis	24
2.4.1 Pressure, Temperature and Nozzle Size Dependence	25
2.5 Characterization of Clusters	30
2.5.1 Rayleigh Scattering	31
Chapter 3 Applications	
3.1 Atmospheric Case - Shock Diamonds	38
3.2 Argon Icy Filament Generation	42
3.3 Multi-nozzle Gas Jets	45
References	49

## List of Figures

- Figure 1.1: Various mass-limited targets developed at UMD suitable for high-repetition-rate laser-driven HDEP experiments: (a) atomic cluster nanoparticles scattering off incident green laser light, (a') cluster gas jets imaged by interferometry, (b) microdroplet source, (b') two streams of micron-sized liquid droplets near their vertical turning point. The larger droplets are  $\sim 30 \mu\text{m}$  in diameter, (c) argon fiber with diameter of  $< 90 \mu\text{m}$  produced from a cryogenically cooled capillary tube, (c') imaging of Ar fiber continuously produced from the capillary orifice. 1
- Figure 1.2: Comparison of nozzle design between the converging-diverging de Laval nozzle and straight capillary nozzle. 2
- Figure 2.1: (a) Image of how the capillary tubes are soldered onto the brass cap (b) Microscopic view of nozzle tubes. (c) Image of the manufactured and commercial nozzles with exit diameter of  $100 \mu\text{m}$ ,  $150 \mu\text{m}$ ,  $250 \mu\text{m}$ ,  $350 \mu\text{m}$ , and  $450 \mu\text{m}$  from left to right. 10
- Figure 2.2: Schematic of the experimental setup that depicts a vacuum chamber with three ports and the nozzle placed at the center. 12
- Figure 2.3: The interference pattern produced from the two beams recombined from the two arms of the interferometer. The blue rectangle represents the area imaged by the CCD camera. 13
- Figure 2.4: Diagram and schematic of the copper block with one pipe carrying the gas (argon or nitrogen) into the copper block, circling and passing through it three times, and the other pipe carrying the liquid nitrogen to cool the copper block to the desired temperature. 16
- Figure 2.5: Characteristic gas density profiles showing the interferogram and corresponding phase profile of argon gas using nozzle of inner diameter  $150 \mu\text{m}$  and backing pressures of  $69 \text{ bar}$  at (a) room temperature operation,  $293 \text{ K}$ , and (b) cooled at  $173 \text{ K}$ , producing clusters, and (c) cooled at  $133 \text{ K}$ , producing argon droplets. 20

Figure 2.6: Schematic representation of the measurement of an axisymmetric distribution of relative index of refraction, $\eta(r, y) - 1$ and the accumulated phase shift $(x, y)$ of a light ray traversing the distribution, represented by the integral of the relative refractive index along the path travelled through it.	22
Figure 2.7: Number density profiles for argon gas jets produced using 55 bar backing pressure at 193K with nozzle of inner diameter of (a) 50 $\mu\text{m}$ , (b) 100 $\mu\text{m}$ , (c) 150 $\mu\text{m}$ , (d) 250 $\mu\text{m}$ , (e) 350 $\mu\text{m}$ , and (f) 450 $\mu\text{m}$ respectively right above the tip of the nozzle.	24
Figure 2.8: Maximum on-axis argon gas density produced with various nozzles of inner diameter (a) 450 $\mu\text{m}$ , (b) 350 $\mu\text{m}$ , (c) 250 $\mu\text{m}$ , (d) 150 $\mu\text{m}$ , (e) 100 $\mu\text{m}$ , and (f) 50 $\mu\text{m}$ at backing pressures of 13.7-69.0 bar and at 153-293 K temperatures.	26
Figure 2.9: Density lineouts of argon gas jet using 150 $\mu\text{m}$ ID nozzle with backing pressure of 69 bar at a height of 50 $\mu\text{m}$ above the orifice for various block temperatures.	27
Figure 2.10: Peak number density as a function of the gas jet backing pressure showing a linear relation.	27
Figure 2.11: Peak on-axis gas density as a function of nozzle inner diameters at various backing pressures of 13.8-69.0 bar at room temperature in the gas reservoir.	28
Figure 2.12: Background pressure of the vacuum chamber as argon gas is continuously pumped through the capillary nozzles of various (a) backing pressures and (b) nozzle exit diameters operated at room temperature.	29
Figure 2.13: CCD images of Rayleigh scattered light from argon gas produced with the 150- $\mu\text{m}$ (ID) capillary nozzle at 50 $\mu\text{m}$ height above the orifice at room temperature for backing pressures of (a) 34.5 bar, (b) 37.9 bar, (c) 41.4 bar, (d) 44.8 bar, (e) 48.3 bar, (f) 51.7 bar, (g) 55.2 bar, (h) 58.6 bar, (i) 62.1, (j) 65.5, and (k) 68.9 bar.	34
Figure 2.14: The relative scattered energy from the gas target with respect to the gas jet backing pressure for argon gas jet using 150 $\mu\text{m}$ exit diameter capillary nozzle at various block temperatures.	35

Figure 2.15: Height scan of the Rayleigh scattering profile of argon gas at 69 bar at room temperature using the 250 $\mu\text{m}$ exit diameter capillary nozzle.	36
Figure 3.1: Difference in phase profiles of gas jets produced with the argon at backing pressure of 69 bar using a 150 $\mu\text{m}$ exit diameter nozzle at room temperature for (a) atmospheric case of 750 Torr background pressure and (b) in vacuum of 70 mTorr.	38
Figure 3.2: Structure of a moderately underexpanded jet illustrating the parts of the shock diamond.	39
Figure 3.3: Shock diamond structure produced by argon gas jet using the 150 $\mu\text{m}$ exit diameter nozzle at 14 bars backing pressure to atmospheric pressure and room temperature.	39
Figure 3.4: Comparison between the measured distance of the first shock diamond above the nozzle orifice and the theoretical values for both the argon and nitrogen gas jet generated with the 150 $\mu\text{m}$ exit diameter nozzle at 14 bars backing pressure to atmospheric pressure and room temperature.	40
Figure 3.5: Pressure-temperature phase diagram of argon where the red circled region represent the regime where argon filaments were observed to form as reported by Peth.	41
Figure 3.6: One second interval shadowgraph images of the icy fiber target produced with argon using 100 $\mu\text{m}$ inner diameter nozzle cooled to 110 K and backing pressure of 5 bar.	42
Figure 3.7: a) The phase shift profile of argon gas using 50 bar backing pressure at room temperature for five nozzles of inner diameter of 100 $\mu\text{m}$ and wall thickness of 75 $\mu\text{m}$ . (b) Photograph of the manufactured multi-nozzle array.	45
Figure 3.8: Schematic of the femtosecond pump and probe beams to image the shadowgram and interferogram of a corrugated plasma channel produced in the multi-jet array gas jet in continuous flow with $\sim 30$ fs, 800 nm, 10 mJ laser pulses at 1 kHz repetition rate.	48

# Chapter 1. Introduction

## 1.1 Motivation and Outline

We have developed and used various types of mass-limited targets suitable for studying laser-produced high-energy density plasmas. These targets include gases of nano-sized atomic/molecular clusters, micron-sized liquid droplets, and thin solid argon fibers continuously produced from a cryogenically cooled capillary tube. There are various applications for high density gas jets including x-ray generation, high-repetition-rate (>1 kHz) HEDP experiments, and ion/proton acceleration density ramp <sup>[1][2]</sup>.

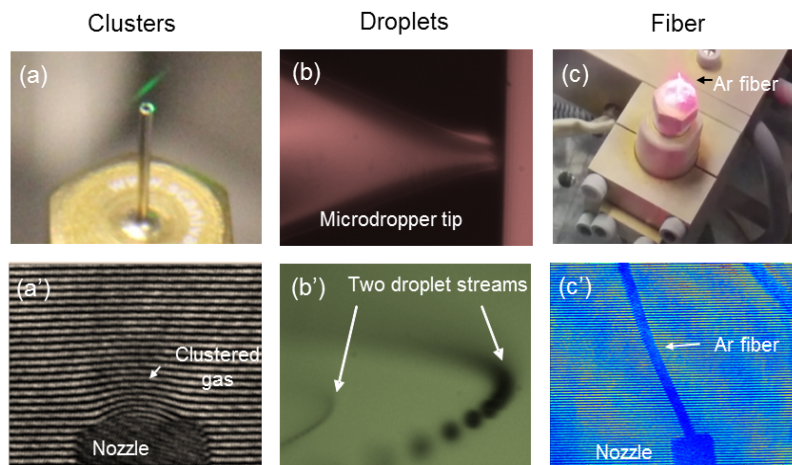


Figure 1.1: Various mass-limited targets developed at UMD suitable for high-repetition-rate laser-driven HEDP experiments: (a) atomic cluster nanoparticles scattering off incident green laser light, (a') cluster gas jets imaged by interferometry, (b) microdroplet source, (b') two streams of micron-sized liquid droplets near their vertical turning point. The larger droplets are  $\sim 30 \mu\text{m}$  in diameter, (c) argon fiber with diameter of  $< 90 \mu\text{m}$  produced from a cryogenically cooled capillary tube, (c') imaging of Ar fiber continuously produced from the capillary orifice.

Supersonic gas jets are employed to provide the particular gas density profiles for the laser-plasma interaction experiments [3]. A supersonic gas jet is a flow of gas, travelling at a velocity greater than the speed of sound, emanating from an orifice, called the nozzle. The nozzle is shaped such that one is able to control the properties of the gas jet, most importantly the density. Because supersonic gas jets offer a large degree of control over the gas density, they are very suitable for use as targets in laser-plasma interaction experiments. In order to illustrate to what degree one can control the density distribution in a supersonic gas jet, it is important to understand the nature of the flow inside a supersonic nozzle. Different type of nozzles can be used to produce gas targets for laser plasma experiments, including the de Laval nozzles shown in Figure 1.2, which has a convergent-divergent shape throat diameter and exit diameter. For narrower targets, straight capillary nozzles provide a good density profile due to the smaller expansion of the gas jet. Cylindrical nozzles have advantages where high-density and short gas target are required, and the laser beam is focused close to the nozzle output area. The supersonic de Laval nozzles have advantages where more extended flat profiles with modest gas concentration and long focusing length of the laser beam are implemented [4].

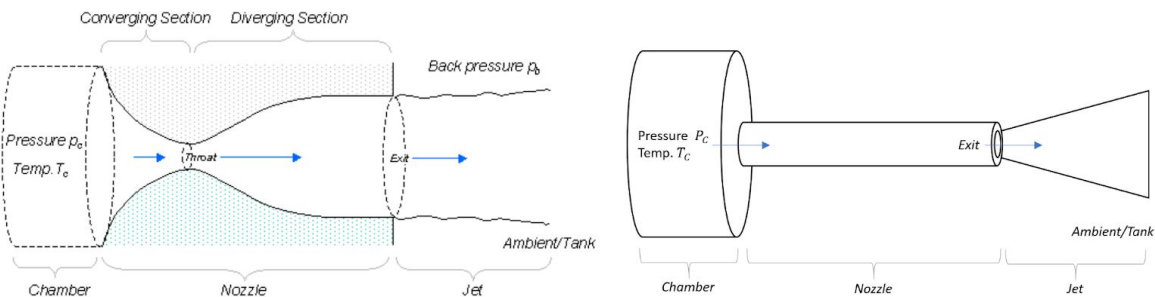


Figure 1.2: Comparison of nozzle design between the converging-diverging de Laval nozzle and straight capillary nozzle.

The first step, in providing a brief overview of gas flow, is determining the thermodynamic properties and relations relevant to the flow of an ideal gas, after which a continuum approach is followed to construct a framework for determining the kinetic behaviour of the gas flow, neglecting viscous effects and conductive heat transfer. Because the gas is flowing at velocities equal to and above the speed of sound it is essential to take into account effects of compressibility of the gas. The development of this framework is covered in Section 1.2. Having introduced the various concepts regarding compressible gas flows an analysis of the flow in a supersonic nozzle is given. Analytical solutions are available to quasi one-dimensional flows and a connection is made between the flow inside the supersonic nozzle and the gas jet plume emanating from this nozzle. For the gas and vacuum pressures commonly encountered in laser-plasma experiments, the gas jet emanating from a supersonic nozzle will be in the underexpanded regime, resulting in the appearance of a structure of shocks in the jet plume. Due to the high pressures and low temperatures encountered in supersonic expansions, gas particles can aggregate and form clusters of atoms or molecules.

The focus of this thesis is on designing and characterizing suitable plasma targets for density gradient injection in laser wakefield acceleration, which is outlined in Section 1.3. The critical electronic density  $n_c$  of a plasma irradiated by a Ti:Sapphire laser beam of central wavelength  $\lambda = 800 \text{ nm}$  is  $1.68 \times 10^{21} \text{ cm}^{-3}$  and sets in the non-relativistic case the density limit above which the electromagnetic wave cannot propagate. Therefore, these targets need to provide densities high enough also with sharp density gradients, with widths

of either 100 to 300  $\mu\text{m}$  for injection via wave breaking, or 1 to 10  $\mu\text{m}$  for injection by rephasing.

## 1.2 Supersonic Gas Jets - Flow Physics

The physics of the flow and the gas behaviour as it passes through the nozzle is crucial in determining the density distribution in a supersonic gas jet. This section aims to provide an understanding of the thermodynamic properties and relations relevant to the flow of an ideal gas. In local thermodynamic equilibrium, all thermodynamic properties of a homogeneous and isotropic one-component medium are completely determined by the variables pressure  $p$ , temperature  $T$ , and volumetric mass density  $\rho$ . The relation between the pressure, temperature and density of a medium is given by the equation of state. Using the equation of state, two variables are always sufficient to determine the thermodynamic state of the system. For an ideal gas the equation of state is formed by the ideal gas law, with  $R$  the ideal gas constant and  $M$  the molar mass of the medium as <sup>[5]</sup>

$$p = \frac{\rho RT}{M} . \quad (1.1)$$

The density of the medium can also be expressed as the number of particles in a volume. The resulting particle density  $n$  is related to the volumetric mass density by

$$n = \rho \frac{N_A}{M} , \quad (1.2)$$

where  $N_A$  is the Avogadro constant. The constant reflects that an ideal gas at standard temperature and pressure of 298 K, 1 atm has a particle density of  $2.5 \times 10^{19} \text{ cm}^{-3}$ . For laser-plasma interaction experiments, expressing the density in terms of number of particles per volume is more convenient than using the amount of mass enclosed in a volume. This is

because, after ionization of the gas, the resulting electron density in the plasma is directly related to the particle density of the neutral gas [6].

The gas density at the nozzle exit is primarily determined by the exhaust gas velocity, which is affected by the geometry of the nozzle that changes the expansion conditions inside it. This section will examine the flow parameters using the 1DIFF model to predict for an ideal gas through a system of equations linking the cross-sectional area  $A$  to the density  $\rho$  and the Mach number parameter.

The compressible flow equations used to calculate the behavior of the pressure  $P$  and density  $\rho$  inside the nozzle are given by

$$\frac{P}{P_o} = \left[1 + \frac{\gamma-1}{2} M^2\right]^{\frac{\gamma}{\gamma-1}}, \quad (1.3)$$

$$\frac{\rho}{\rho_o} = \left[1 + \frac{\gamma-1}{2} M^2\right]^{\frac{\gamma}{\gamma-1}}, \quad (1.4)$$

where  $P_o, \rho_o$  are the critical values of pressure and density where gas flow turns from subsonic to supersonic flow,  $\gamma$  is the adiabatic exponent and  $M$  is the Mach number defined as the ratio of the speed of the flow to the speed of sound [7].

### 1.3 Laser Wakefield Acceleration

Laser wakefield accelerators were first proposed in 1979 by Tajima and Dawson [8], and with advances in laser technology since then, compact systems for generating laser intensities high enough to efficiently drive nonlinear plasma waves became readily available,

and laser based acceleration experiments were performed by research groups world-wide. For laser wakefield acceleration, an ultra-short high-intensity laser pulse is sent into a plasma. The force on the plasma due to the laser radiation pressure is often described as the ponderomotive force. As the laser pulse travels through the plasma, electrons are expelled from its path by the ponderomotive force, which is independent of the sign of the particle charge and always act to expel charges from regions of high intensity, while the ions remain at an almost fixed position due to their higher mass.

After the laser pulse has passed, the electrons are pulled back to their original position by the Coulomb force resulting from the charge separation. The electrons, however, overshoot their initial position due to their momentum, thereby creating an oscillating electron density modulation travelling in the wake of the laser pulse. This oscillation creates a longitudinal charge separation wave, called a plasma wave, trailing the laser pulse. Associated with the charge separations in such a plasma wave are extremely large longitudinal electric fields, forming the wakefield trailing the laser pulse. The presence of these large longitudinal electric fields, thousands of times higher than encountered in conventional accelerators, is what makes laser wakefield acceleration a promising candidate for next-generation particle accelerators. When an electron bunch is properly injected into this wakefield it can be accelerated to ultra-relativistic energies over distances thousands of times shorter than in conventional accelerators.

## **Chapter 2. Gas Jet Characterization**

Manufacturing nozzles can be a challenge especially ones with thin diameters and in a manner that will minimize the number and size of imperfections on the nozzle wall and exit lip. The materials used and manufacturing process is explored in Section 2.1. The experimental setup is detailed in Section 2.2 including the characterization of the gas jets using a Mach-Zehnder interferometer (Section 2.2.1). The nozzles were mounted into a vacuum chamber that operated under conditions comparable to those in the laser-plasma experiments (Section 2.2.2) and in order to reach higher gas density levels, cooling to 133 K was achieved using liquid nitrogen and a copper cooling block (Section 2.2.3). Section 2.3 covers the numerical methods used, including fast Fourier transforms, FFT (Section 2.3.1) and Abel Inversion (Section 2.3.2) used to determine the neutral densities produced from the gas jets. The results of the density profiles and trends with respect to temperature, backing pressure and nozzle sizes are explored in Section 2.4. And clusters were studied through scattering in Section 2.5 using Rayleigh scattering techniques (Section 2.5.1) to characterize the clusters in the target.

### **2.1 Nozzles**

Even though the goal of this experiment is to generate thin and dense gas jets using straight capillary nozzles, de Laval nozzles are the most commonly used geometry for generating supersonic gas jets in laser-plasma experiments due to their flat-top density profiles and steep density gradients at the jet edges.

### 2.1.1 Manufacturing Straight Capillary Nozzle

Gas jet nozzles for laser wakefield acceleration may be fabricated from various materials resistant to the harsh operational conditions using different subtractive and additive technologies. There are several ways of manufacturing nozzles such as hybrid 3D laser machining technique from fused silica using the nanosecond rear-side processing approach which have reported achieving output diameters of 100-500  $\mu\text{m}$  [9]. The conventional method of CNC machining from metals is time-consuming and is not suitable for fabricating complex structures with a high aspect ratio (structure depth to width ratio). Laser based stereolithography methods allow rapid manufacturing from plastics of custom-shaped nozzles down to 100  $\mu\text{m}$  exit diameter at a low cost [10]. However, additional post-processing is required to open the blocked nozzle, and the materials are of moderate resistance. Also, in the sub-millimeter scale, the printed holes fail in maintaining the circular shape, and the achievable aspect ratio is close to one.

Glassy materials are an alternative due to the hardness of the material and manufacturing flexibility. However, conventional mechanical drilling of glass suffers from limitations in hole aspect ratio (typically up to 10:1), achievable minimum hole diameter (on the order of 100  $\mu\text{m}$ ), low machining quality and relatively slow processing speed [11]. Another effective method uses liquid-assisted femtosecond laser drilling of high aspect ratio holes (50:1) at the speed of several of  $\mu\text{m}/\text{s}$  from the rear side of the glass. When water is used, it removes debris continuously away from the holes and therefore the drilling process is equally efficient with following pulses. The drilling depth was mainly limited by the accumulation and redeposition of the processing debris.

The parameter study described in the following uses a commercial straight capillary nozzle of orifice diameter 50  $\mu\text{m}$ , 100  $\mu\text{m}$ , 150  $\mu\text{m}$ , 250  $\mu\text{m}$ , 350  $\mu\text{m}$  and 450  $\mu\text{m}$ , some of which were machined. The capillary tubes had to be mounted on a threaded high-pressure brass cap that was initially drilled to make a hole slightly bigger than the outer diameter of the capillary tubes to go through. It is an extremely precise process and for the smaller capillary tubes, cobalt micro drill bits ( $\sim 200 \mu\text{m}$ ) were mounted on a guided milling machine to slowly peck at the brass cap. The debris from the drilling had to be removed constantly to ensure the surface is smooth. The stainless steel capillary tubes were then cut to appropriate lengths and both sides were smoothed so that the gas can pass through without blockages. Once the capillary tube is held in place in the drilled hole, it is soldered onto the brass cap and then checked for leakages while being able to obtain a supersonic outflow.

The nozzles with inner diameter 150  $\mu\text{m}$  (4406T33), 250  $\mu\text{m}$  (4406T34), and 350  $\mu\text{m}$  (4406T35) were commercially available from McMaster-Carr and are stainless steel high-pressure tube fittings that functioned well for our purposes. The brass caps in which all the nozzles were attached on had 1/8" NPT threads which allows it to be mounted on the copper cooling block.

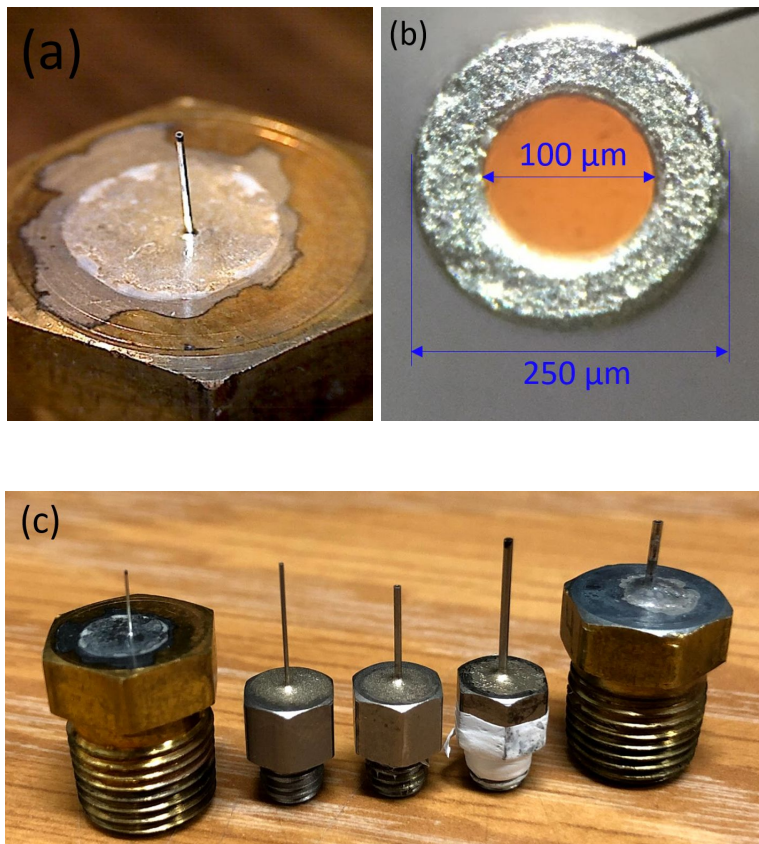


Figure 2.1: (a) Image of how the capillary tubes are soldered onto the brass cap. (b) Microscopic view of nozzle tubes. (c) Image of the manufactured and commercial nozzles with exit diameter of 100 μm, 150 μm, 250 μm, 350 μm, and 450 μm from left to right.

## 2.2 Experimental Setup

### 2.2.1 Mach-Zehnder Interferometer

The neutral gas density profile in a gas jet is measured with a Mach-Zehnder type interferometer using a CW diode laser (633 nm, 5mW) as shown in Figure 2.2. The probe beam paths are shown by the red lines in the figure. The laser light traversing through the gas jet experiences a phase shift due to the refractive index variation  $\Delta n(x, y, z)$  imposed by the gas density profile. First the CW diode laser beam is expanded to a diameter of 2 cm using a telescope. After picking up a phase shift in the gas jet, the laser beam is relay-imaged by two lenses ( $f_1 = 25$  cm,  $f_2 = 50$  cm) onto a charge-coupled device (CCD) camera in the Mach-Zehnder interferometer located outside the vacuum chamber. Inside the interferometer, the laser beam is split into two and then recombined to form interference fringes on the CCD camera (14 bit, Stingray F-125) providing resolution of 1292 x 964 pixels. The spatial resolution used for the different nozzle sizes ranges from 0.75  $\mu\text{m}$  to 1.5  $\mu\text{m}$ . In our experiment, the interferometer stands outside the vacuum chamber, and the laser beam is split after picking up a phase in the gas jet, which is different from a conventional interferometric method <sup>[12]</sup>. The difference between conventional Mach Zehnder interferometer and what was used here is that one beam passes through the gas jet before being split and recombined to produce the fringe patterns. Conventionally, the expanded beam is first split into two where one arm is sent through the gas target and then combined with the other which is used as a reference. The disadvantage of that setup is that both arms need to travel the same distance and becomes a challenge with all the optics that each beam have to travel.

During alignment for the interferometry, the interference fringes was adjusted to be horizontal as seen in Figure 2.3. The interferometer also sits on top of a rubber mat to reduce vibrations and produce more stable interferograms for measurements. Without the mat, the interference fringes are sensitive to any slight motion on the optical table which made phase extraction difficult. With stable fringes, long exposure of the CCD camera results in enhanced signal-to-noise ratios in the extracted phase profiles. Neutral density (ND) filters were used to decrease the laser intensity t avoid saturation and improve image contrast.

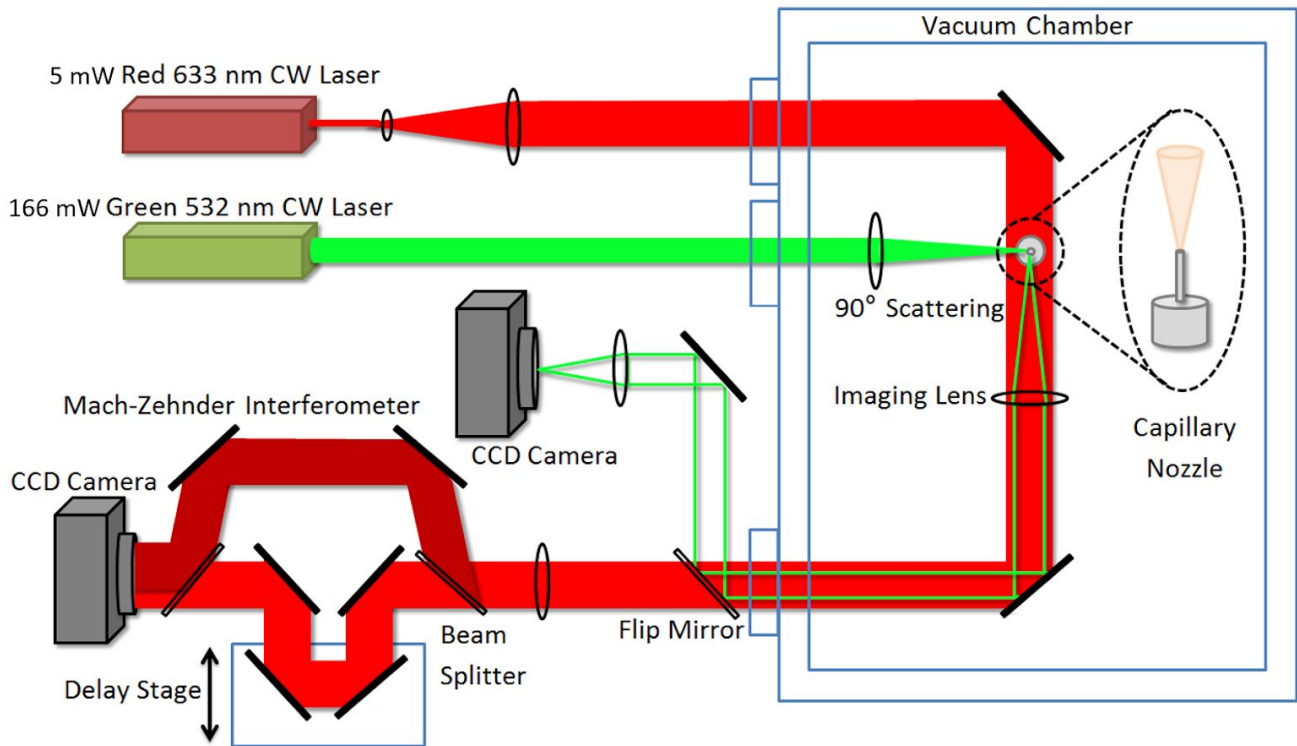


Figure 2.2: Schematic of the experimental setup that depicts a vacuum chamber with three ports and the nozzle placed at the center. This allows both interferometry and Rayleigh scattering data to be collected conveniently.

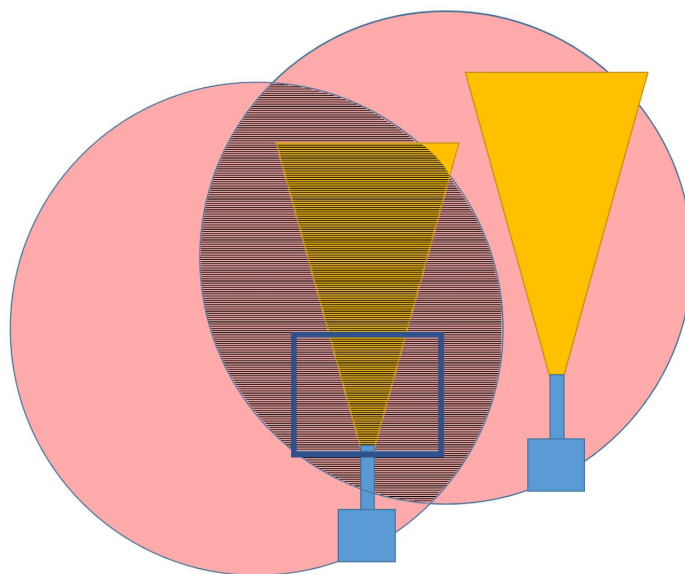


Figure 2.3: The interference pattern produced from the two beams recombined from the two arms of the interferometer. The blue rectangle represents the area imaged by the CCD camera.

In our Rayleigh scattering setup for cluster detection, a 532 nm 166 mW laser beam is focused into the gas jet at a height of 50  $\mu\text{m}$  above the nozzle exit. The focusing of the beam and careful alignment onto the gas target was done to prevent the green beam from reflecting off the tip of the stainless steel nozzle and collect only scattered light from the clusters in the target. The scattered light is collected by a lens with focal length 25 cm located 90° with respect to the probe beam direction because the linearly polarized green light allows for maximum scattering to occur at 90° angles and then imaged on a CCD camera. The scattering results and characterization of clusters are presented in Section 2.5 in detail.

### 2.2.2 Vacuum Chamber

Gas jets would ideally be pumped through the nozzle into a perfect vacuum, but realistic experimental conditions would encounter a certain background pressure. The main contributor to the development of the background pressure would certainly be the gas load of the gas jet itself, and even more so when the gas jets are operated continuously compared to pulsed gas jets.

The gas reservoir body is mounted on a copper cooling cryostat with pipes that provides the necessary gas with liquid nitrogen and thermocouple for temperature control, which is further described in the next section. The copper block is then mounted on a 3-dimensional (3D) stage for translational scans and placed in a vacuum chamber equipped with a dual stage rotary vane vacuum pump (Edwards E2M80) with a peak pumping speed of 53 cfm and 60 Hz. There is also an additional mechanical booster pump (BOC Edwards EH250). The pressure inside the chamber is measured using a convection enhanced Pirani vacuum gauge (Kurt Lesker, KJL 300). As the gauge is calibrated for direct readout of nitrogen, accurate conversion data were applied to measure the background pressure for argon gas targets.

A major concern using a high-density continuous flow gas jet is the background pressure buildup inside the target chamber, which can lead to ionization-induced defocusing of laser pulses prior to reaching the dense target. This effect was studied in a recent experiment on laser wakefield acceleration of electrons where the accelerated electron spectra was measured for increasing valve open times for pulsed gas jets. It is seen that

increasing the valve open time, even at ~20 Torr background pressure, lowers the charge per shot while keeping the normalized spectra similar [13].

The average pressure inside the vacuum chamber is maintained at 0.050 mTorr with full operation of the pumps. It rises during operation of the continuous gas jet depending on the nozzle size and backing pressure used, to a maximum of ~5 Torr with a 450  $\mu\text{m}$  nozzle at 800 psi backing pressure. The vacuum chamber operates below 1 Torr for small nozzles (50  $\mu\text{m}$ , 100  $\mu\text{m}$  and 150  $\mu\text{m}$ ) which are ideal for high-intensity laser interaction with gas jets, including electron acceleration and X-ray generation. The size of the nozzle exit diameter is the main factor for the amount of background pressure the chamber settles at while running both the continuous gas jet and vacuum pumps simultaneously. The chamber background pressure for all nozzle sizes were measured and the effects are explored in Section 2.4.

### **2.2.3 Cooling and Temperature Control**

The nozzle temperature is regulated by cooling and/or heating the copper mounting block. The cooling is done via a copper braid which is mounted with good thermal contact to a very thin walled liquid nitrogen (LN2) filled stainless steel pipe, directly welded to the source mounting flange. The gas target also passes through the copper block on a separate copper braid line with good thermal contact to be cooled down. Figure 2.4 below shows an image of the copper block and a schematic of how the gas target and liquid nitrogen flow in the copper block. There is a heating element and temperature controller which monitors the temperature via a K-type thermocouple mounted on the copper mounting block. For

thermal insulation, we note that a Teflon block is inserted between the 3D stage and the aluminum mount attached to the cooling block as shown in the figure. Note that the temperature of the block is the reservoir temperature for the gas jets in operation.

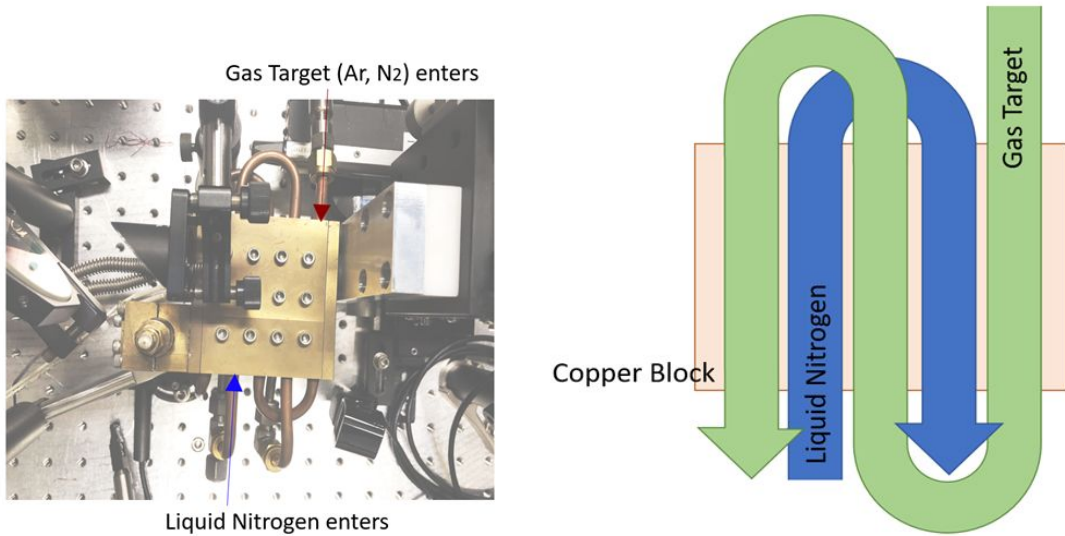


Figure 2.4: Diagram and schematic of the copper block with one pipe carrying the gas (argon or nitrogen) into the copper block, circling and passing through it three times, and the other pipe carrying the liquid nitrogen to cool the copper block to the desired temperature.

## 2.3 Interferometry Analysis

### 2.3.1 Phase Extraction

Using the Mach-Zehnder setup described above, interferograms can be collected to extract the phase information by making use of Fast Fourier Transformation (FFT). The phase shift introduced to the interferometer can be given by

$$\Delta\Phi = \left(\frac{2\pi}{\lambda}\right) \int (n - 1) dl , \quad (2.1)$$

where  $\lambda$  is the probing laser wavelength,  $n$  is the index of refraction of the gas target, and  $\Delta\Phi$  represents the measured phase shift. Using the Gladstone-Dale relationship to relate the index of refraction of a neutral gas to its density results in the following equation

$$\Delta\Phi = kM\left(\frac{2\pi}{\lambda}\right) L , \quad (2.2)$$

where  $k$  is the Gladstone-Dale constant,  $M$  is the atomic mass of the gas, and the line-integrated density  $L = \int N dl$ , where  $N$  is the density of the gas and the integral is performed along the path of the laser through the gas. This can be determined from the bending of the fringes in the presence of a gas target by measuring the shift with respect to reference fringes where no gas is present.

The Fourier transform method developed by Takeda <sup>[14]</sup> notates that the intensity  $I(y, z)$  of a general fringe pattern in the  $z$ -direction can be described using equation

$$I(x, y) = I_A(x, y) + I_B(x, y) \cos(2\pi f_o x + \Phi(x, y)) , \quad (2.3)$$

where  $I_A(x, y)$  represents the background intensity and  $I_B(x, y)$  the variations in the visibility of the fringes. These intensity fluctuations are assumed to vary slowly compared to the modulation introduced by the carrier frequency of the fringes  $f_o$ , which is well satisfied in the experiments due to the low gas index and thickness of the jet.  $\Phi(x, y)$  carries the phase information which is to be retrieved from the fringe pattern because it is related to the particle density of the gas. Rewriting Equation (2.3) using Euler's formula and introducing  $I_C(x, y) = \frac{1}{2}I_B(x, y) e^{i\Phi(x, y)}$  gives

$$I(x, y) = I_A(x, y) + I_C(x, y) e^{i2\pi f_o x} + I_C^*(x, y) e^{-i2\pi f_o x}. \quad (2.4)$$

The fringe pattern given by Equation (2.4) is the Fourier transformed with respect to  $x$ , resulting in the spectrum of the fringe pattern intensity

$$\widehat{I}(f_x, y) = \widehat{I}_A(f_x, y) + \widehat{I}_C(f_x - f_o, y) + \widehat{I}_C^*(f_x + f_o, y). \quad (2.5)$$

Next to the background  $\widehat{I}_A(f_x, y)$  consists of two spectra separated from the zero frequency spectrum by the carrier frequency  $f_o$ . With the use of a filter function, only  $\widehat{I}_C(f_x - f_o, y)$  spectrum is extracted from Equation (2.5) and subsequently be unwrapped. By selecting this spectrum means filtering out all spatial frequency components that are not related to the phase shift resulting from the gas jet, but at the same time be careful to preserve all the information of the gas jet. Filtering to too narrow spectrum results in disappearance of valuable high frequency information.

Finally the phase  $\Phi(x, y)$  and the envelope intensity  $I_B(x, y)$  can be obtained as

$$\Phi(x, y) = \tan^{-1} \frac{\text{Im}[I_C(x, y)]}{\text{Re}[I_C(x, y)]}, \quad (2.6)$$

$$\text{and } I_B(x,y) = 2 \left| I_C(x,y) \right|. \quad (2.7)$$

In order to reduce shot-to-shot fluctuation in the measured interferograms, 30 phase profiles are extracted and averaged from the collected interferograms.

Figure 2.5 shows sample interferograms obtained with our setup with corresponding phase profiles extracted by the FFT method. Figure 2.5 (a) shows a phase profile  $\Phi(x,y)$  obtained with the 150  $\mu\text{m}$  inner diameter nozzle at backing pressure of 69 bar when operated at room temperature. It shows a maximum phase shift of 7.79 rad. Figure 2.5(b) clearly shows that the gas density enhances a lot with cooling evident from a larger phase shift of 13.61 rad. Also at low temperatures, a large amount of atomic clusters or even droplets can be produced along with monomers <sup>[15]</sup>. Those large-sized particles greatly attenuate the probe intensity by scattering, yielding darker background in the jet. This attenuation becomes severe at very low temperatures, resulting in the interference patterns to not be visible and making it difficult to extract the phase profile. Figure 3(c) shows an interferogram of the argon gas jet at a temperature of 133 K obstructing the fringes from view. This is the reason there are missing values for the phase and density plots.

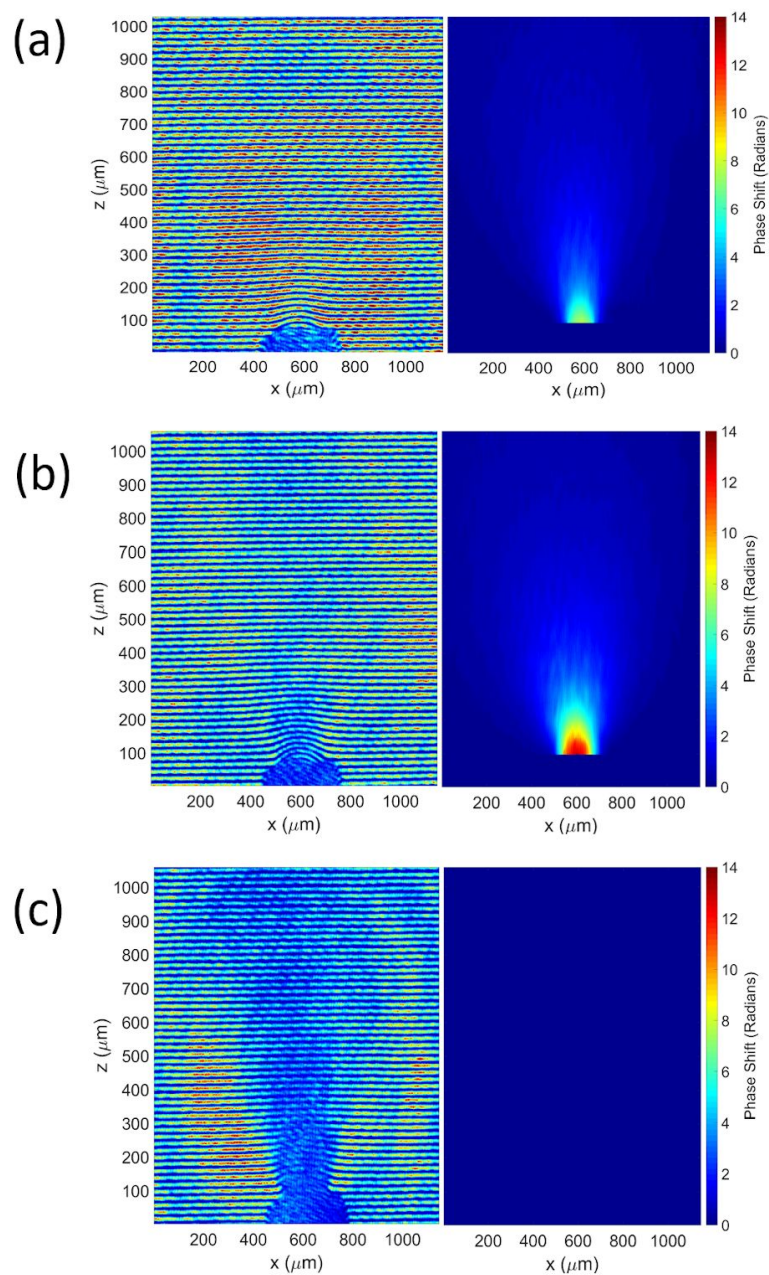


Figure 2.5: Characteristic gas density profiles showing the interferogram and corresponding phase profile of argon gas using nozzle of inner diameter  $150\ \mu\text{m}$  and backing pressures of 69 bar at (a) room temperature operation, 293 K and (b) cooled at 173 K, producing clusters and (c) cooled at 133 K, producing argon droplets.

### 2.3.2 Abel Inversion

The resulting two-dimensional phase data was then Abel-inverted using a numerical Fourier-based algorithm published by G. Pretzler [16] and written by Carsten Killer in MATLAB to extract the 2D radial gas density distribution from a one-dimensional phase projection measurement. Compared to earlier approaches towards Abel Inversion, this algorithm is relatively insensitive to noise and errors in determination of the object's center. The phase images obtained by interferometry are mostly symmetric and as the Abel transform assumes an axisymmetric profile in density (cylindrical symmetry), where the phase images are symmetric with respect to the center of the gas jet. Determination of the center position of the jet was performed using the half-maximum points of the phase shift profile.

With the gas jet illuminated from one side in the interferometric set-up, the obtained phase image of the gas jet is simply a two-dimensional projection of the three-dimensional gas jet. For the case of an axisymmetric gas jet, as we use here, reconstructing the structure of the gas jet is possible using only a single projection measurement. To deduce the relation between the measured phase-shift and the density of the gas jet, consider the geometry depicted in Figure 2.6, where a ray of light is propagating in the positive  $x$ -direction through an axisymmetric gas jet, positioned at the origin in the  $xy$ -plane. The relative refractive index of the gas is assumed to drop to zero at large distances from the origin. The amount of gas the light encounters results in a projection of the refractive index,  $\eta(r, y) - 1$ , of the gas jet onto the  $yz$ -plane. Calculating the accumulated phase shift of the light results in Eq. (2.8), which is known as the Abel transform given by

$$\Phi(x, y) = \frac{2\pi}{\lambda} 2 \int_x^\infty \frac{(\eta-1)r}{\sqrt{r^2-x^2}} dr . \quad (2.8)$$

Inverting Abel transform allows one to retrieve the index of refraction of the gas jet from a measured phase-shift as

$$\eta(\lambda, r, y) - 1 = \frac{\lambda}{2\pi} \frac{1}{\pi} \int_r^\infty \frac{d\Phi(x,y)}{dx} \frac{1}{\sqrt{y^2-r^2}} dx . (2.9)$$

The particle density profile of the gas jet is then obtained by making use of the Lorentz-Lorenz equation as

$$n(r, y) = \frac{-\varepsilon_0 \lambda}{\pi^2 \alpha(\lambda)} \int_r^\infty \frac{d\Phi(x,y)}{dx} \frac{1}{\sqrt{y^2-r^2}} dx . \quad (2.10)$$

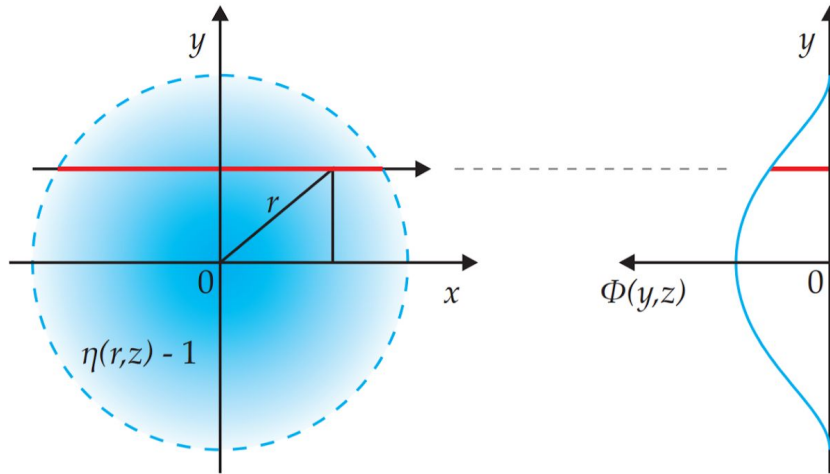


Figure 2.6: Schematic representation of the measurement of an axisymmetric distribution of relative index of refraction,  $\eta(r, y) - 1$  and the accumulated phase shift  $\Phi(x, y)$  of a light ray traversing the distribution, represented by the integral of the relative refractive index along the path travelled through it.

The fundamental idea for Pretzler's numerical method is to fit the whole measured profile to a set of cosine-expansion-based integrals. In contrast, the traditional method obtains the radial distribution by starting at the edges and incrementally iterating towards the center, making it more prone to errors. In general, an axis-symmetric function  $f(r)$  can be expanded as

$$f(r) = \sum_{n=N1}^{Nu} A_n f_n(r), \quad (2.11)$$

with unknown amplitudes  $A_n$  where  $f_n(r)$  is a set of cosine-functions, e.g.

$$f_o(r) = 1, f_n(r) = 1 - (-1)^n \cos(n\pi \frac{r}{R}). \quad (2.12)$$

Following Equation (2.8), the Abel-transform  $H(y)$  of Equation (2.11) has the form

$$H(y) = 2 \sum_{n=N1}^{Nu} A_n \int_y^R f_n(r) \frac{r}{\sqrt{r^2-y^2}} dr, \quad (2.13)$$

with each integral

$$h_n(y) = \int_y^R f_n(r) \frac{r}{\sqrt{r^2-y^2}} dr, \quad (2.14)$$

having been integrated numerically in advance and stored on a special file. Equation (2.13)

is least squares fitted to the real data  $h(y)$  at each of the  $N$  measured points  $y_k$

$$\sum_{k=1}^N (H(y_k) - h(y_k))^2 \rightarrow \min, \quad (2.15)$$

leading to

$$\sum_{n=N1}^{Nu} A_n \sum_{k=1}^N (h_n(y_k) h_m(y_k)) = \sum_{k=1}^N (h(y_k) h_m(y_k)). \quad (2.16)$$

## 2.4 Results and Analysis

Using the Abel Inversion method and the phase profile measured from the interferometry, the density profiles were determined. Two of the smaller nozzles (i.e. 50  $\mu\text{m}$  and 100  $\mu\text{m}$ ) produced interferograms with small phase shifts, making it difficult to calculate the density profiles numerically. In this case, the phase profiles were fitted to a Gaussian curve before being Abel Inverted to remove noise and achieve characteristic.

Figure 2.7 shows extracted number density profiles  $N(r,y)$  for argon using six different nozzle diameters at backing pressure of 55 bar at 193 K. This is the best density profile at the nozzle exit while avoiding any possibilities of ablating or melting the nozzle caused by any intense laser contact or damage from laser accelerated particles. Here the same scale bar is applied for better comparison. Some oscillatory features are observed for large size nozzles and could be an artifact from the Abel Inversion process, which will be explored in more detail in the following section.

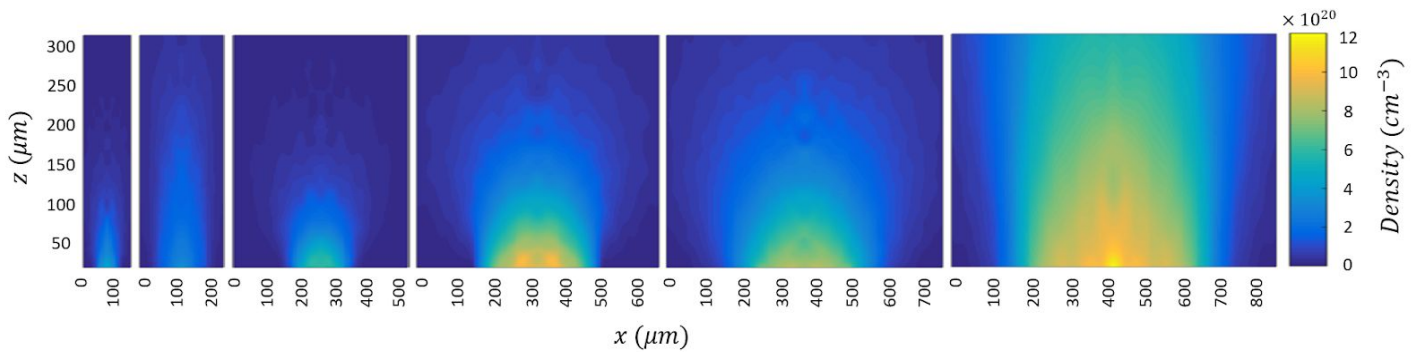


Figure 2.7: Number density profiles for argon gas jets produced using 55 bar backing pressure at 193K with nozzle of inner diameter of (a) 50  $\mu\text{m}$ , (b) 100  $\mu\text{m}$ , (c) 150  $\mu\text{m}$ , (d) 250  $\mu\text{m}$ , (e) 350  $\mu\text{m}$ , and (f) 450  $\mu\text{m}$  respectively right above the tip of the nozzle.

### 2.4.1 Pressure, Temperature and Nozzle Size Dependence

Figure 2.8 shows a collection of peak density values for six different nozzle diameters (a) 50  $\mu\text{m}$ , (b) 100  $\mu\text{m}$ , (c) 150  $\mu\text{m}$ , (d) 250  $\mu\text{m}$ , (e) 350  $\mu\text{m}$ , and (f) 450  $\mu\text{m}$  respectively. The peak densities are determined by averaging over an area just above the nozzle orifice to obtain a gas density number that represent peak number density. It can be seen that the peak gas density increases with decreasing temperature and with increasing backing pressure. Some points are missing for the larger nozzles for low temperatures and higher backing pressures due to the target condensing to droplets near the nozzle orifice as seen in Figure 2.5 where the interferogram lines are difficult to distinguish and a phase profile was not able to be extracted. It can be assumed that the density value at those points would be higher and follows the trends observed.

It can be seen from the density lineouts that there are oscillations but a quantitative analysis of the gas density profiles can be carried out by averaging the value in the flat-top part of the density. The highest density for Argon achieved with nozzles of inner diameter 150  $\mu\text{m}$  near the exit of the nozzle using backing pressure of 69 bar is  $4.99 \times 10^{20} \text{ cm}^{-3}$  at room temperature, which can be enhanced to  $8.12 \times 10^{20} \text{ cm}^{-3}$  with cooling down to 153 K. It can also be seen in Figure 2.9 that the density lineouts show a flat top profile with a sharp boundary that increases as temperature of the gas reservoir decreases. For lower pressure and/or smaller nozzle exit diameter, the gradient width at the jet edge gets wider and the profiles becomes more gaussian-like.

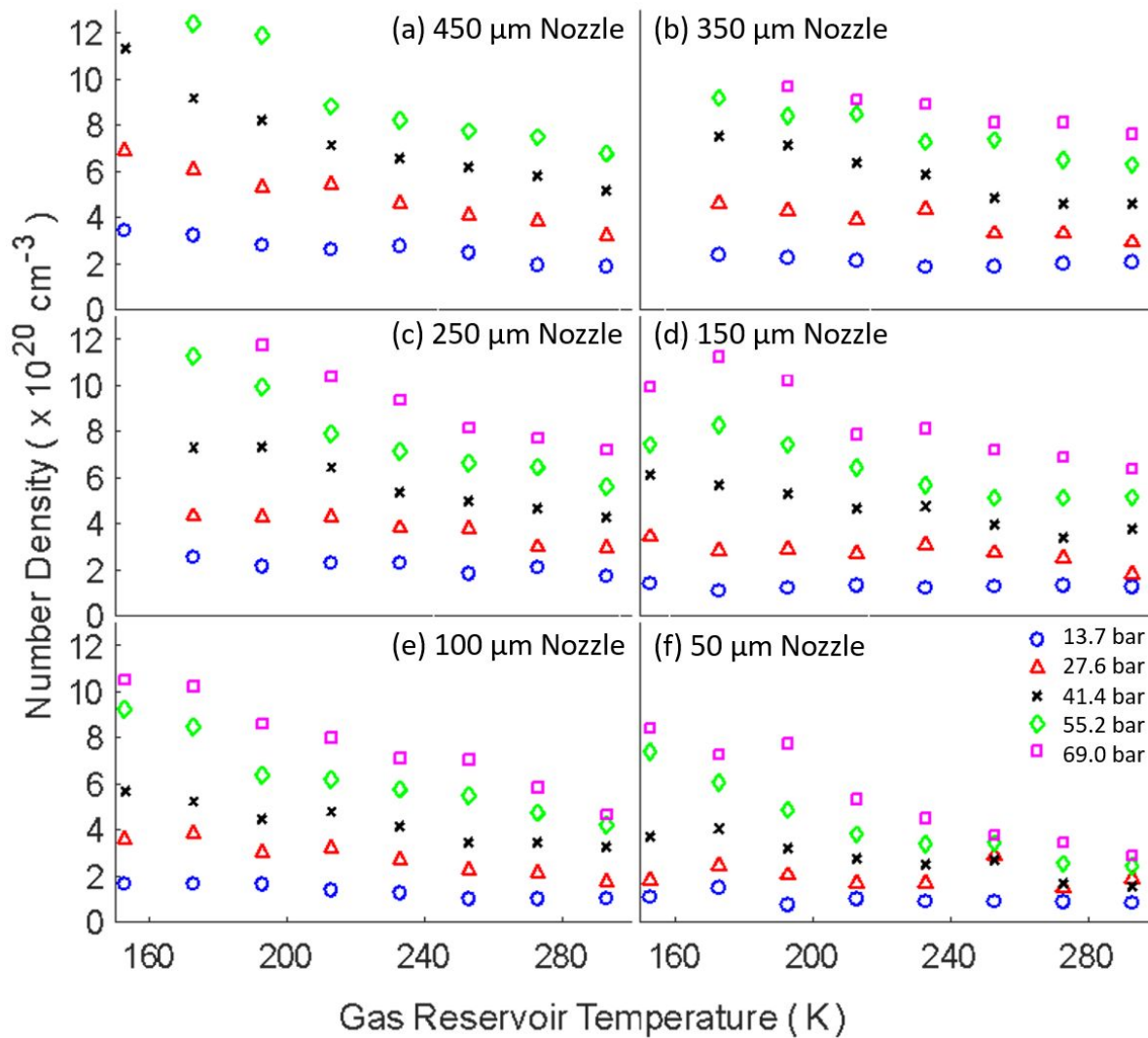


Figure 2.8: Maximum on-axis argon gas density produced with various nozzles of inner diameter (a) 450  $\mu\text{m}$ , (b) 350  $\mu\text{m}$ , (c) 250  $\mu\text{m}$ , (d) 150  $\mu\text{m}$ , (e) 100  $\mu\text{m}$ , and (f) 50  $\mu\text{m}$  at backing pressures of 13.7-69.0 bar and at 153-293 K temperatures.

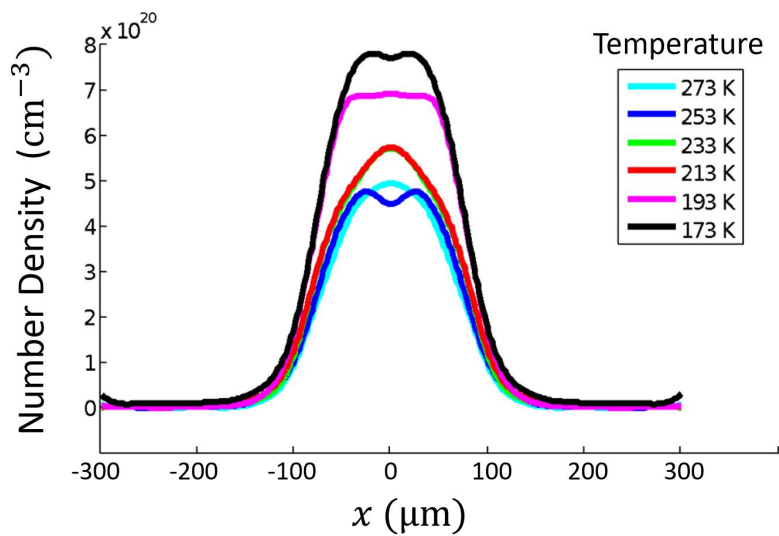


Figure 2.9: Density lineouts of argon gas jet using 150  $\mu\text{m}$  ID nozzle with backing pressure of 69 bar at a height of 50  $\mu\text{m}$  above the orifice for various block temperatures.

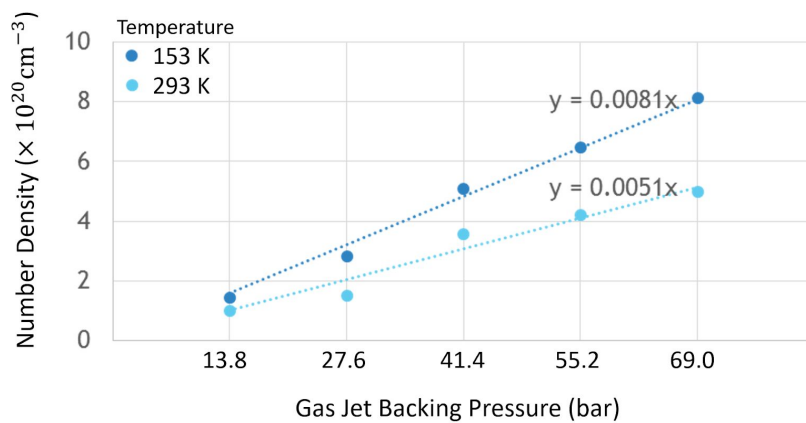


Figure 2.10: Peak number density as a function of the gas jet backing pressure showing a linear relation.

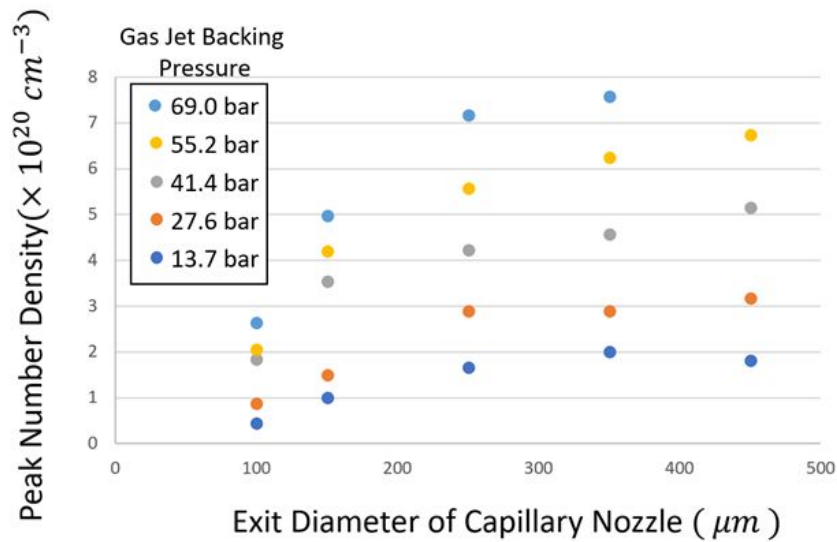


Figure 2.11: Peak on-axis gas density as a function of nozzle inner diameters at various backing pressures of 13.8-69.0 bar at room temperature in the gas reservoir.

In Fig. 2.10, it can be seen that the peak gas density produced by the nozzle has a linear relationship with respect to backing pressure for all block temperature. However, if the temperature is halved the density-pressure slope doesn't exactly double in magnitude.

Figure 2.12 shows our measurements of the background pressure inside the vacuum chamber as a function of gas backing pressure for various inner diameters of nozzles. It clearly shows that the background pressure increases almost linearly with the backing pressure. Also, the background pressure increases quadratically with the nozzle diameter as seen in Figure 2.12(b), and this is because the cross-sectional area of a nozzle is proportional to  $r^2$ . We note that the thinnest nozzle provides background pressures of no greater than 0.5 Torr even at 69 bar backing pressure.

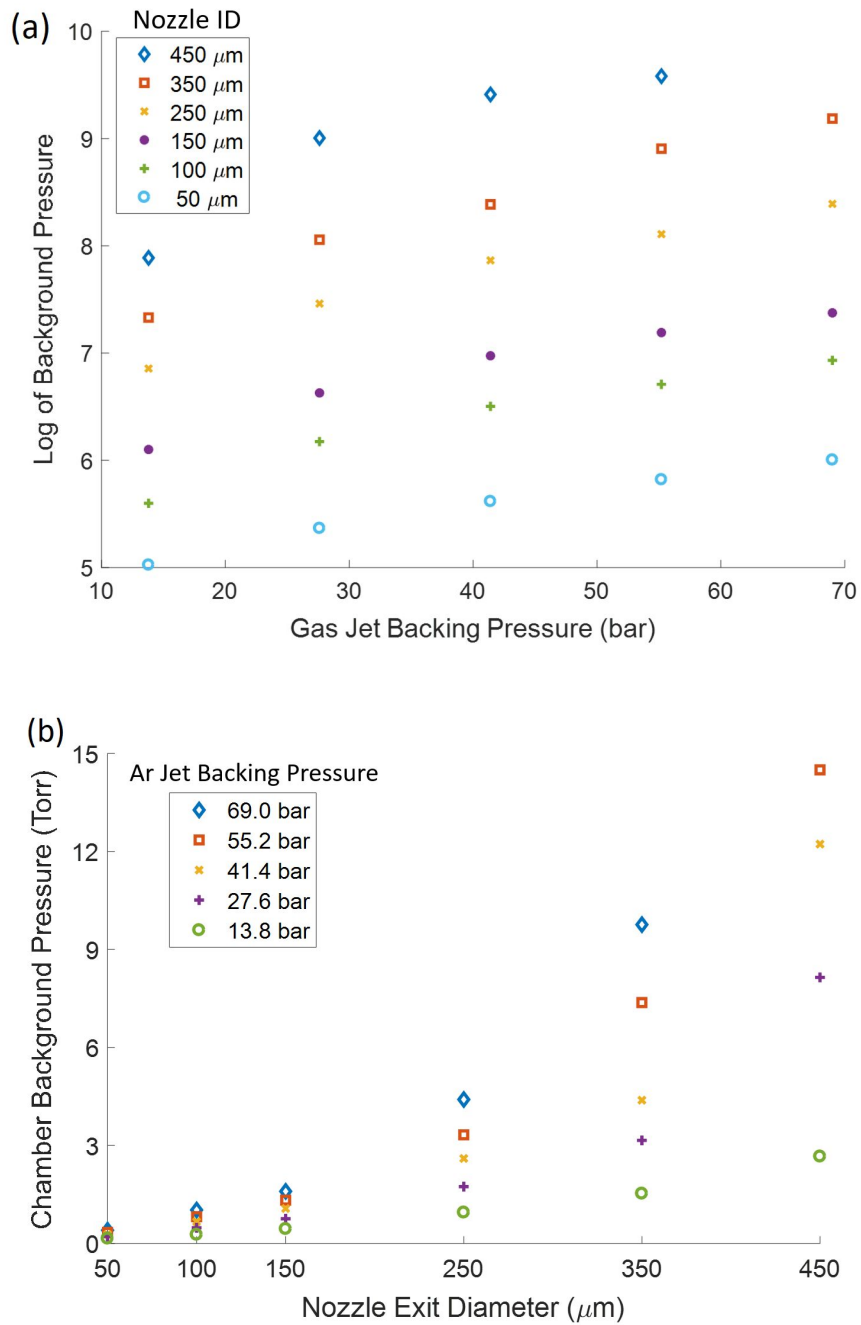


Figure 2.12: Background pressure of the vacuum chamber as argon gas is continuously pumped through the capillary nozzles of various (a) backing pressures and (b) nozzle exit diameters operated at room temperature.

## 2.5 Characterization of Clusters

Cluster formation occurs when a highly pressurized gas undergoes a rapid expansion through a nozzle into vacuum. At high valve backing pressure, atoms or molecules experience collisions in the initial expanding phase where the collisional mean free path is much smaller than the nozzle diameter. This occurs as the adiabatic expansion of the working gas in the nozzle flow result in its supercooling, and in this supercooled gas the enclosures of the condensed phase (clusters) are produced as a result of the spontaneous condensation [17]. Here Van der Waals forces lead to the formation of dimers which seeds the initial cluster nucleation and the collisions further the cluster growth [18].

Atomic or molecular clusters, van de Waals- bonded aggregates of up to  $\sim 10^7$  atoms, make unique targets for laser matter interaction because it allows an intense laser pulse propagating through a gas of clusters microscopically to interact with nanoscale solids while macroscopically propagating through a gaseous environment for an extended interaction. For example, cluster containing jets can be efficient targets for attosecond extreme ultraviolet (XUV) pulses and high harmonics generation (HHG) [19].

The average number of atoms in a single cluster is traditionally characterized by a semi-empirical formula proposed by Hagena [20]. The Hagena parameter is given by

$$\Gamma^* = k \frac{P_o d^{0.85}}{T^{2.29}}, \quad (2.17)$$

where  $P$  is the backing pressure,  $T$  is the pre-expansion temperature,  $k$  is a constant that is gas specific ( $k \sim 1650$  for Ar) and  $d$  is the parameter for the nozzle geometry in  $\mu\text{m}$ . The

geometry of the nozzles has an important role for the efficiency of cluster formation, and for supersonic conical nozzle with a jet expansion half angle of  $\alpha$ , an equivalent diameter  $d_{eq} = 0.74d/\tan \alpha$  can be used. However, for straight cylindrical nozzles,  $d$  will just be the inner diameter of the capillary tubes which the gas exits. The dimensionless  $\Gamma^*$  is then related to the average number of atoms per cluster,  $n_c$  given by [18]

$$\langle n_c \rangle = 33 \left( \frac{\Gamma^*}{1000} \right)^{2.35} \quad (\text{for } \Gamma^* > 1000), \quad (2.18)$$

and the average cluster size in the frame of liquid drop model is

$$a = r_{WS} n_c^{1/3}, \quad (2.19)$$

where the Wigner-Seitz radius is  $r_{WS} = (3m/4\pi\rho)^{1/3}$  for a given mass,  $m$  and atom bulk density,  $\rho$  in the liquid state at the melting point. This shows that we can control the average number of atoms in clusters by varying the nozzle geometry, gas species, and jet temperature and backing pressure [21].

### 2.5.1 Rayleigh Scattering

Laser-induced Rayleigh scattering can be an effective diagnostic tool in investigating gas properties, especially verifying the presence of clusters in gas jets. Cluster size measurements are conducted on the principle that the intensity of light elastically scattered by a particle or an object is related to its size [12]. Here the scattering regime is characterized by the relative size of the scattering particle with radius  $r$  with respect to the laser wavelength  $\lambda$ , given by

$$x = \frac{2\pi r}{\lambda} . \quad (2.20)$$

If  $x \ll 1$ , Rayleigh scattering dominates as the size of the scattering object is much less than the wavelength of the laser. For  $x \approx 1$ , Mie scattering occurs and the phase variation from the object's surface induces interference in the scattered light. When the object is relatively large ( $x \gg 1$ ), scattered light is treated classically and is simply related to the projected area of the scatterer. In the Rayleigh regime, the scattering cross section for a spherical cluster with cluster radius  $r$ , laser of wavelength  $\lambda$  and index of refraction of cluster medium,  $\eta$  is given by

$$\sigma_{scatt.} \propto \frac{r^6}{\lambda^4} \left( \frac{\eta^2 - 1}{\eta^2 + 2} \right) . \quad (2.21)$$

In our Rayleigh scattering setup for cluster detection, a 532 nm 166 mW laser beam is focused into the gas jet at a height of 50  $\mu\text{m}$  above the nozzle exit. The laser beam is carefully aligned so that it only interacts with the gas and does not hit the nozzle. The scattered light is collected by a lens with focal length 25 cm located 90° with respect to the probe beam direction and then imaged on a CCD camera. Figure 2.13 shows sample images of 90° Rayleigh scattering at several gas jet backing pressures.

The relative scattered energy from the gas target is plotted in Figure 2.14 with respect to the gas jet backing pressure. Here each data point is obtained by integrating all scattered light from Figure 2.13. A polynomial least squares fit applied to each scan shows a strong nonlinear dependence with both pressure and temperature. This nonlinear trend indicates the presence of clusters in the gas jet. If there is no clusters present in the gas jet, then the Rayleigh scattering signal would be linearly proportional to the gas backing

pressure. However, if clusters are present and their sizes increase with the backing pressure according to Hagena's semi-empirical law in Eq. (2.17), then the scattering signal becomes proportional to <sup>[20]</sup>

$$S_{Rayleigh} \propto N_C \sigma_{scatt.} \propto (N_o/n_c)(n_c^2) \propto p^{3.35}. \quad (2.21)$$

Our measurements are not in perfect agreement with Hagena's scaling law, but their nonlinear scaling strongly suggest that clustering occurs in our gas jets. Furthermore, the scattering signal is also nonlinearly dependent of the nozzle temperature. This is also expected from Equation (2.17). This indicates that more clustering occurs with higher gas pressure and lower temperature. Note that Rayleigh scattering is useful in checking the presence of clusters but cannot alone determine the cluster size. In general, a combination of Rayleigh scattering and interferometric imaging can determine the average cluster size and density assuming there is no monomers present <sup>[21]</sup>. Recently, our group demonstrated that a full combination of forward/backward Mie scattering detection, 90° scattering, and interferometry can determine all three parameters--the average cluster size  $a$ , density  $N_C$ , and cluster/monomer ratio  $\delta$  <sup>[22]</sup>.

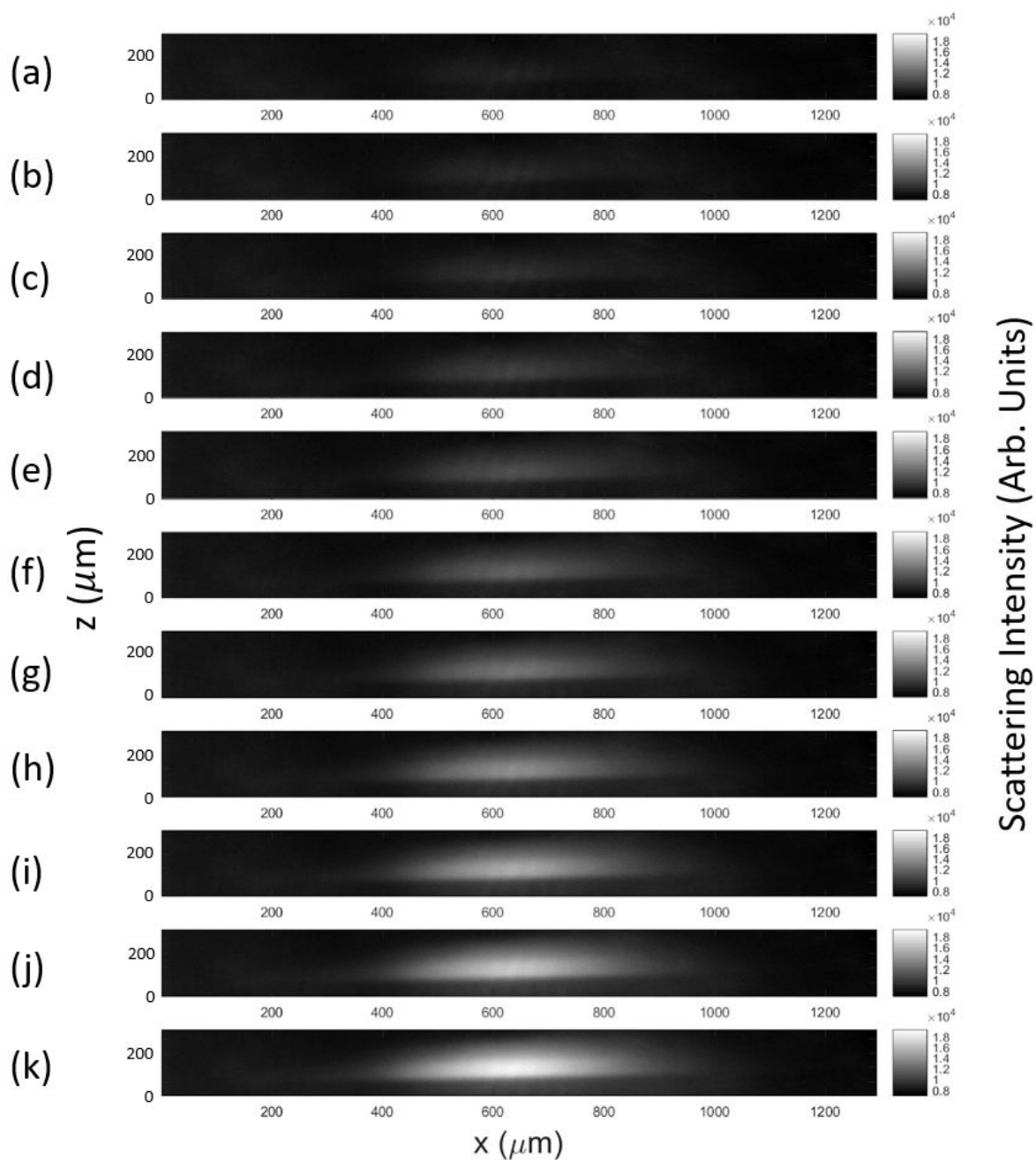


Figure 2.13: CCD images of Rayleigh scattered light from argon gas produced with the 150- $\mu\text{m}$  (ID) capillary nozzle at 50  $\mu\text{m}$  height above the orifice at room temperature for backing pressures of (a) 34.5 bar, (b) 37.9 bar, (c) 41.4 bar, (d) 44.8 bar, (e) 48.3 bar, (f) 51.7 bar, (g) 55.2 bar, (h) 58.6 bar, (i) 62.1, (j) 65.5, and (k) 68.9 bar.

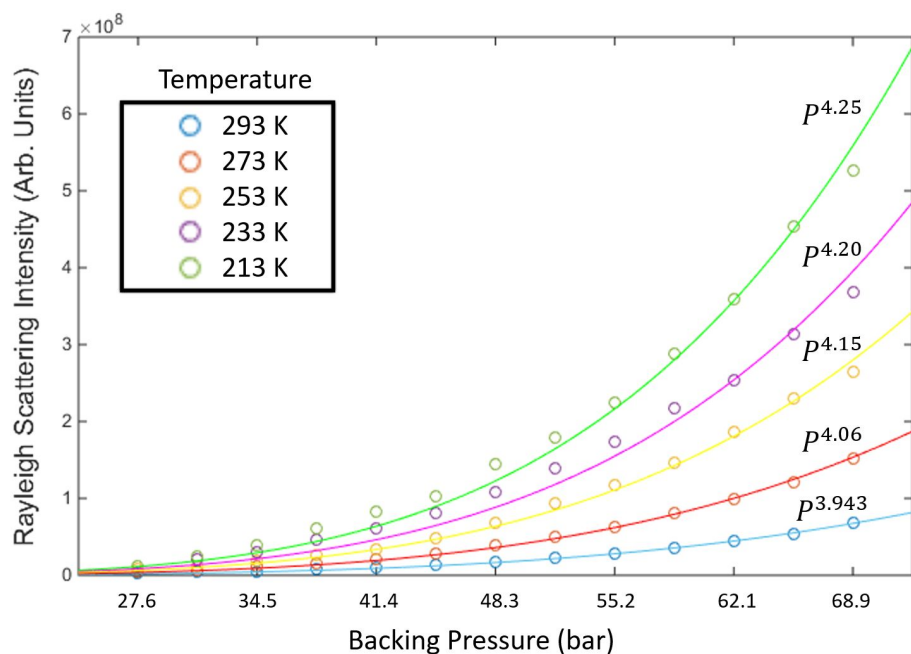


Figure 2.14: The relative scattered energy from the gas target with respect to the gas jet backing pressure for argon gas jet using 150  $\mu\text{m}$  exit diameter capillary nozzle at various block temperatures.

In order to visualize how cluster formation varies above the nozzle, the gas jet is raster scanned by a motorized actuator in the z-axis while the laser beam is fixed. Figure 2.15 shows the 90 degree scattering profile along the beam axis at various heights above the nozzle tip. It can be seen that the highest amount of scattering occurs on-axis at 0.3 mm above the nozzle orifice. As clustering is a relatively slow process, some distance is needed for condensation. This is why for the capillary nozzle — in which case the expansion starts only at the orifice — the cluster size reaches the maximum value farther from the exit.

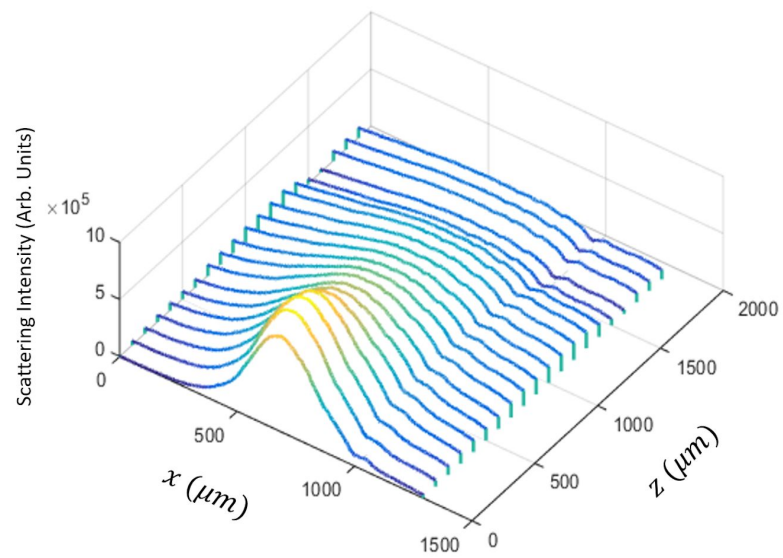


Figure 2.15: Height scan of the Rayleigh scattering profile of argon gas at 69 bar at room temperature using the 250  $\mu\text{m}$  exit diameter capillary nozzle.

## Chapter 3. Applications

The gas jets generated from the straight capillary nozzles can be used in various applications. In Section 3.1 we discuss the operation of gas jets in atmosphere instead of a vacuum and study shock diamond structures formed in this case. As seen in the previous chapter, the gas jets condensates to form clusters and droplets in low temperatures. Section 3.2 demonstrates that under certain circumstances, the gas jet can become icy filament targets with solid densities, which allows many potential applications. Having the capillary nozzles arranged a line can produce multi-jet arrays. This produces density modulations along laser propagation, which in principle can be used to satisfy phase matching in electron acceleration and high harmonic generation. Our method of multi-jet array generation and characterization is detailed in Section 3.3.

### 3.1 Atmospheric Case - Shock Diamonds

High-density gas jets formed in atmospheric air can be of great interest for many practical applications that require compact experimental conditions without any need for vacuum systems. One difference between gas jets in vacuum and atmospheric gas jets is the shapes and densities they manifest as seen in Figure 3.1. Unlike vacuum gas jets, atmospheric jets form shock diamonds very close to the jet orifice due to the large background pressure compared to vacuum [\[23\]](#) .

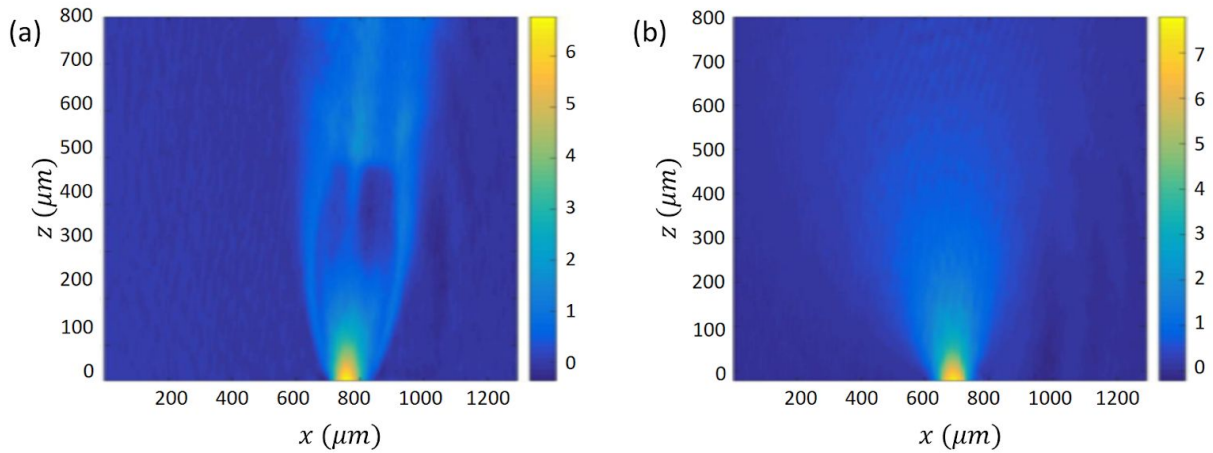


Figure 3.1: Difference in phase profiles of gas jets produced with the argon at backing pressure of 69 bar using a 150  $\mu\text{m}$  exit diameter nozzle at room temperature for (a) atmospheric case of 750 Torr background pressure and (b) in vacuum of 70 mTorr.

Shock diamond structures are a formation of standing wave patterns that appear in the supersonic exhaust plume from a nozzle that is slightly overexpanded or underexpanded. This occurs when the pressure of the gases exiting the nozzle is different from the ambient air pressure which will either expand or compress the flow. Overexpanded flow is compressed while underexpanded flow expands. As seen in Figure 3.1, the Prandtl-Meyer expansion fan expands the gas downstream of the lips of the device upto the jet boundary corresponding to the external surface of the mixing layer. These acoustic waves attain the constant pressure streamline, where the pressure equals the ambient pressure, and are reflected into compression waves. Then, they converge towards the inner jet and coalesce to form an oblique shock, usually called the intercepting shock. On the axis, this incident shock itself reflects in a new oblique shock, the reflected shock, facing the outer jet [\[24\]](#).

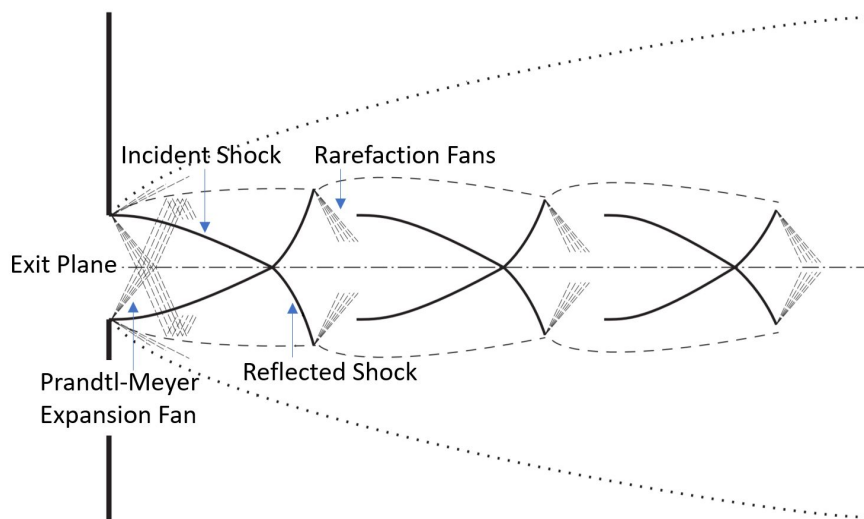


Figure 3.2: Structure of a moderately underexpanded jet illustrating the parts of the shock diamond.

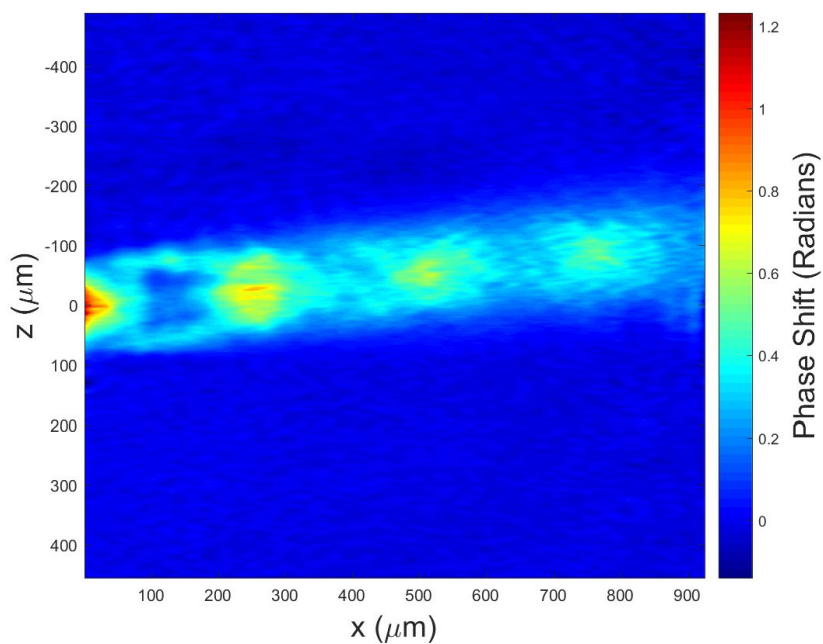


Figure 3.3: Shock diamond structure produced by argon gas jet using the 150  $\mu\text{m}$  exit diameter nozzle at 14 bars backing pressure to atmospheric pressure and room temperature.

The distance from the orifice to the first shock diamond can be approximated by

$$x = 0.67 D_o \sqrt{\frac{P_o}{P_1}}, \quad (3.1)$$

where  $x$  is the distance,  $D_o$  is the nozzle inner diameter,  $P_o$  is flow pressure and  $P_1$  is atmospheric pressure. Using the characteristic gas jet profile for both argon and nitrogen, it can be seen in Figure 3.4 that the measured distance of the first shock diamond above the nozzle orifice and the theoretical values are consistent.

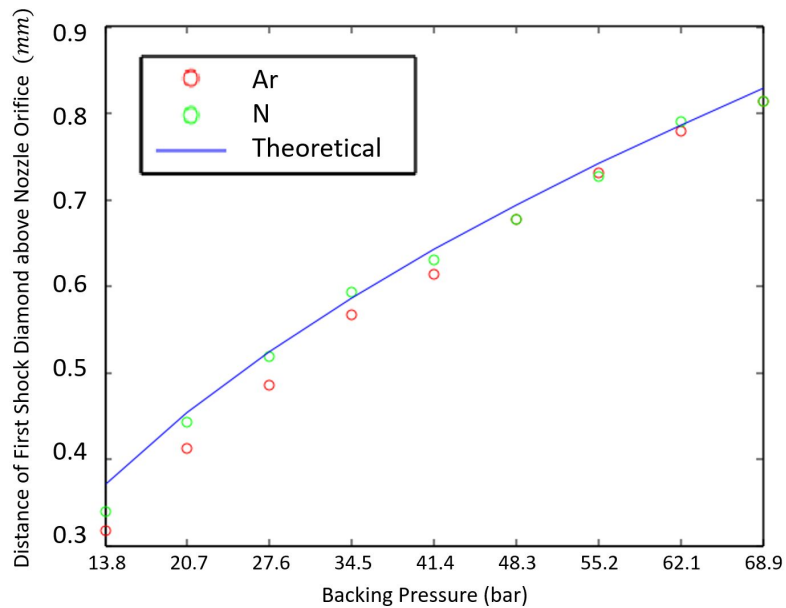


Figure 3.4: Comparison between the measured distance of the first shock diamond above the nozzle orifice and the theoretical values for both the argon and nitrogen gas jet generated with the 150  $\mu\text{m}$  exit diameter nozzle at 14 bars backing pressure to atmospheric pressure and room temperature.

### 3.2 Argon Icy Filament Generation

High-density solid targets are also promising candidates for novel studies including intense laser-driven plasma generation. In our experiment with manufactured straight cylindrical nozzles, cooling an argon gas to low temperature results in an interesting phenomenon. At 110 K with a 100  $\mu\text{m}$  inner diameter nozzle, the argon appears to emerge from the orifice as an icy fiber instead of a gaseous or droplet phase.

Based on the phase diagram of argon shown in Figure 3.5, the melting/freezing temperature is 83.8 K for the pressure being applied. This temperature is much lower than that in the reservoir where the argon gas passes through. However, due to the adiabatic expansion that occurs as the argon exits the nozzle orifice into the vacuum chamber, the target freezes and produces an icy filament.

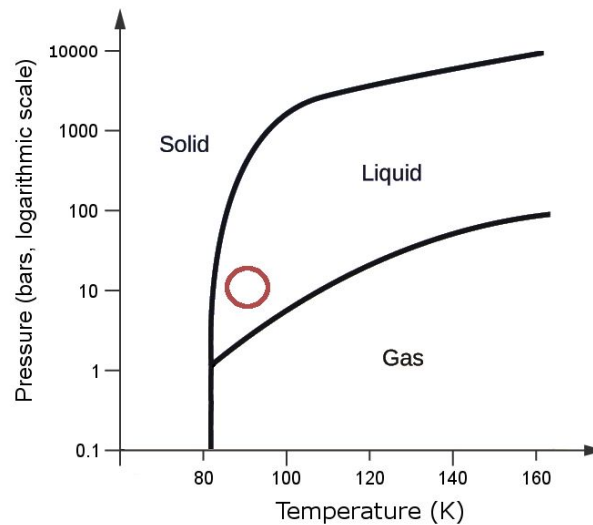


Figure 3.5: Pressure-temperature phase diagram of argon where the red circled region represent the regime where argon filaments were observed to form as reported by Peth [\[25\]](#)

Figure 3.6 shows image frames at 1 second intervals of the argon target as the argon gas passes through the nozzle and undergoes adiabatic cooling at the orifice. The icy filament starts off with an irregular shape but quickly straightens out. However, after a certain period, the icy fiber appears to collapse on its own weight and resets itself. Although interferometric imaging is applied, there are no fringes observed inside the fiber structure due to its near solid density. The thickness of the icy fiber is close to that of the inner diameter of the capillary nozzle of  $100\ \mu\text{m}$  and such a thin high-density target would be of potential interest for relativistic laser-plasma interactions and applications.

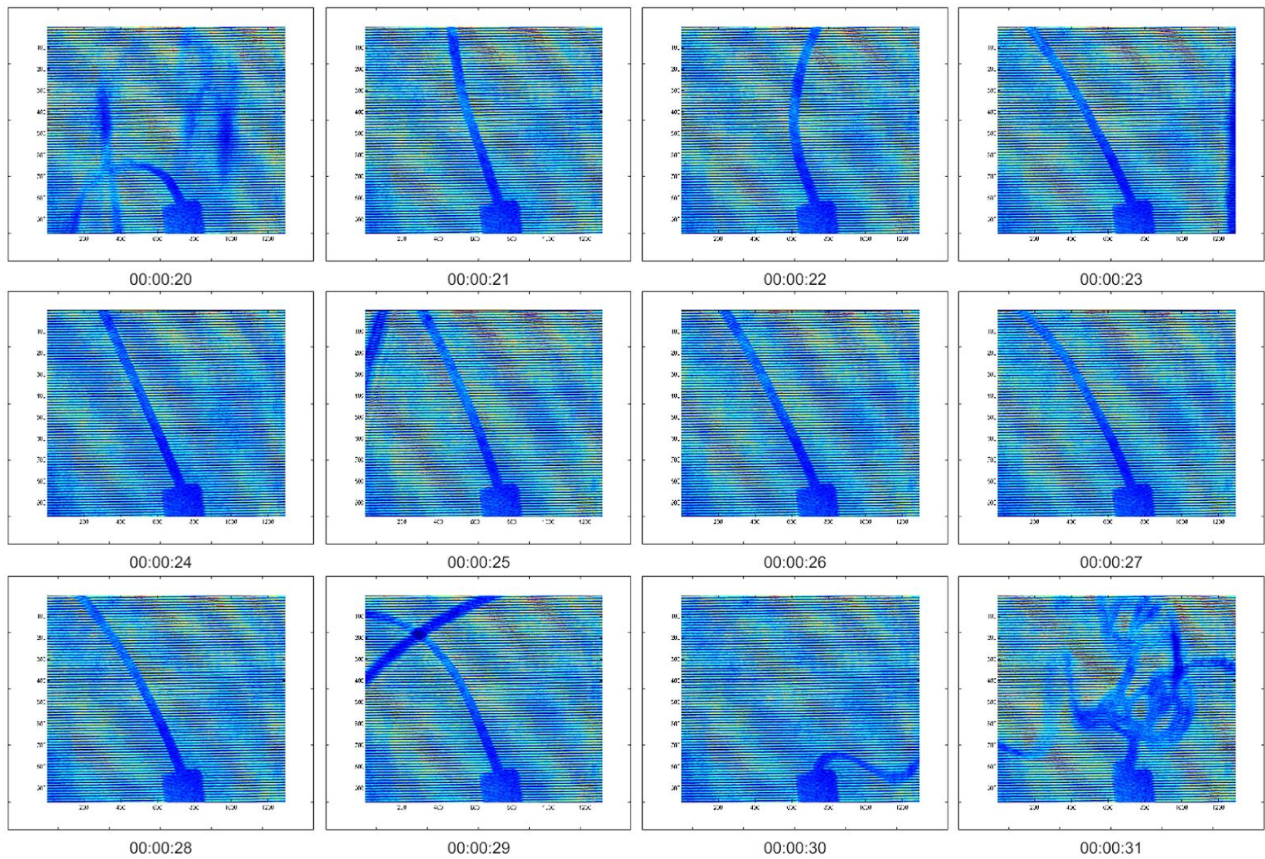


Figure 3.6: One second interval shadowgraph images of the icy fiber target produced with argon using  $100\ \mu\text{m}$  inner diameter nozzle cooled to  $110\ \text{K}$  and backing pressure of  $5\ \text{bar}$ .

One advantage of such a continuous icy filament target is that it can be used for high-repetition-rate laser experiments. This largely contrasts to other solid targets, for example, levitated spherical targets in a Pauli trap, where the employed target must be replaced after each laser shot. Consequently, that process greatly precludes detailed parametric studies requiring the collection of large amount of data, and the use of laser-driven ion sources operating in the quasi-continuous mode that is mandatory for most potential applications. It can also be seen that the icy fibers maintained a smooth constant diameter while it remained upright, which allows for shot to shot variation experiments to take place.

There are, however, several problems with the icy fiber targets and room for improvement. Firstly, the icy filament target is unstable and volatile in the sense that it requires delicate control and is often difficult to maintain for long periods of time. One possible solution is to have a vacuum suction above the nozzle to direct the icy fiber straight up and also prevent it from bending as the length increases over time. The nozzle could also be inverted and have the icy fibers be produced in a downward direction to overcome this issue. Nozzle clogging is also a problem that arises when the temperature gets too low. In this case, the gas freezes inside the nozzle, resulting in no flow through the orifice.

### 3.3 Multi-nozzle Gas Jets

Multi-jet gas puff targets are produced by pulsed injection of gas through a nozzle in a form of chain of small orifices. It has been shown that the use of an array of gas jets with periodic modulation of the gas density enhances the yield of high-order harmonics generation [26]. This behavior may be attributed to a quasi-phase matching (QPM) effect which increase the length of coherent harmonic buildup during propagation by partially counteracting the dephasing induced by free electrons [27].

There are different ways of producing axially modulated plasma waveguides such as flow obstruction by thin wires [28] and puffing gas through laser drilled holes in a gas-filled metal tube [26]. In the first method, the gas flow is modulated by a periodically spaced array of wires near the nozzle exit. In our experiment, we have used an array of five identical stainless steel capillary tubes (ID = 100  $\mu\text{m}$ , OD = 250  $\mu\text{m}$ ) soldered into a drilled brass plug cap as shown in Figure 3.7(b). This nozzle array is tested with argon at various backing pressures, and the interferometric imaging technique described in Section 2.3 is applied to characterize resulting gas profiles. Figure 3.7(a) shows a 2D phase profile extracted from an interferogram taken at room temperature with argon gas jet at 50 bar backing pressure. Five primary jets are clearly seen at the bottom of the phase profile. Interestingly, the primary jets are merged as they flow, forming secondary jets in between two primary jets. Even a tertiary jet is formed in between two secondary jets. Here the ratio of the inner diameter (100  $\mu\text{m}$ ) to the spacing between jets (150  $\mu\text{m}$ ) are important to form secondary and tertiary jets. According to our phase profile, the spacing between the third and fourth primary jets is a bit larger than others, which results in a weaker secondary jet in between them. Also the

fourth and fifth tubes have bad orifice conditions and produce much weaker jets. This is why less pronounced secondary and tertiary jets are formed from the fourth and fifth nozzles. This could be due to inconsistencies during the machining process and the flow through those nozzles were impeded.

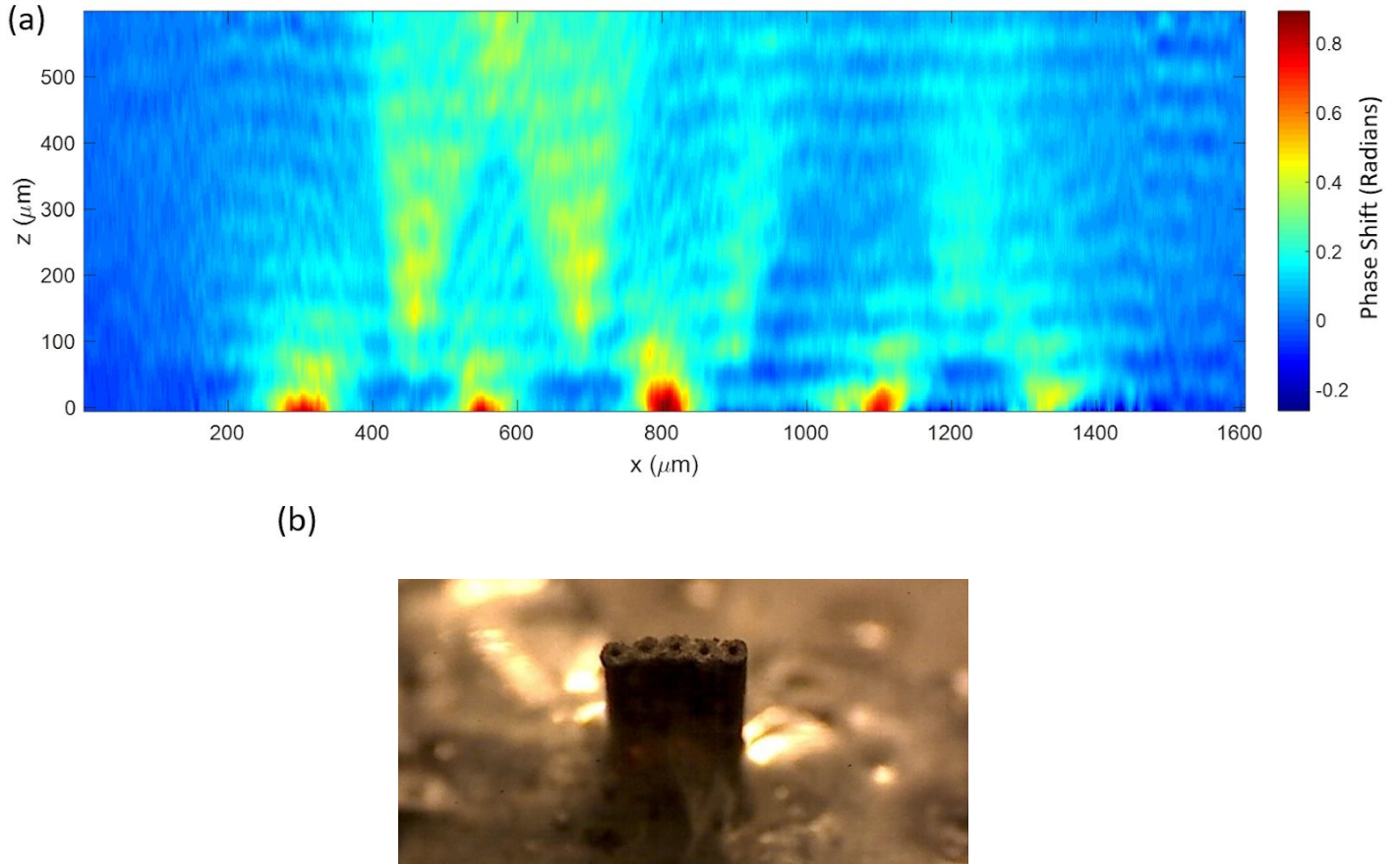


Figure 3.7: (a) The phase shift profile of argon gas using 50 bar backing pressure at room temperature for five nozzles of inner diameter of 100 μm and wall thickness of 75 μm. (b) Photograph of the manufactured multi-nozzle array used.

Note that due to the non-axisymmetric nature of the multi-jet array, Abel Inversion cannot be applied to extract the overall density profiles here. We believe that the primary jets near the nozzles are cylindrically symmetric for each, but the secondary and tertiary jets may not have cylindrical symmetries as they arise from merging of two separately axisymmetric flows. In principle, a tomographic method utilizing multiple projections at many different angles can be applied to reconstruct the exact 3D density profile.

One application of the straight capillary tubes is to arrange multiple tubes in a row to produce the modulated gas target which can achieve specific lengths in principle by connecting more nozzles [29]. The gaps are limited by thickness of the nozzle walls and modulation period dependent on size of the nozzle orifice. Figure 3.8 shows a schematic of the femtosecond pump and probe beams to image the shadowgram and interferogram of a corrugated plasma channel. The corrugated plasma channel was produced in the multi-jet array gas jet in continuous flow with  $\sim 30$  fs, 800 nm, 10 mJ laser pulses at 1 kHz repetition rate. Detailed characterization of target density is essential to increase energy conversion efficiency for QPM in HHG. Other methods such as extreme ultraviolet tomography have been employed by combining shadowgraphy projection images into a 3-D reconstruction volume [30].

These extremely dense and thin gas jets fabricated in this thesis have applications in laser-plasma acceleration of high energy electron beams to the  $\sim 10$  MeV scale using ultrashort laser pulses with as little energy as 10 mJ [31]. As the laser pulse propagates in an underdense plasma, the ponderomotive force pushes electrons away from regions with high electromagnetic field gradient driving longitudinal electron density waves (laser wakefield)

and electrons are accelerated due to the charge separation generated in the plasma. The various parameters to control specific gas densities for targets in laser plasma experiments and potential in developing clusters, icy filament and multijet arrays demonstrated the applications of straight capillary nozzles.

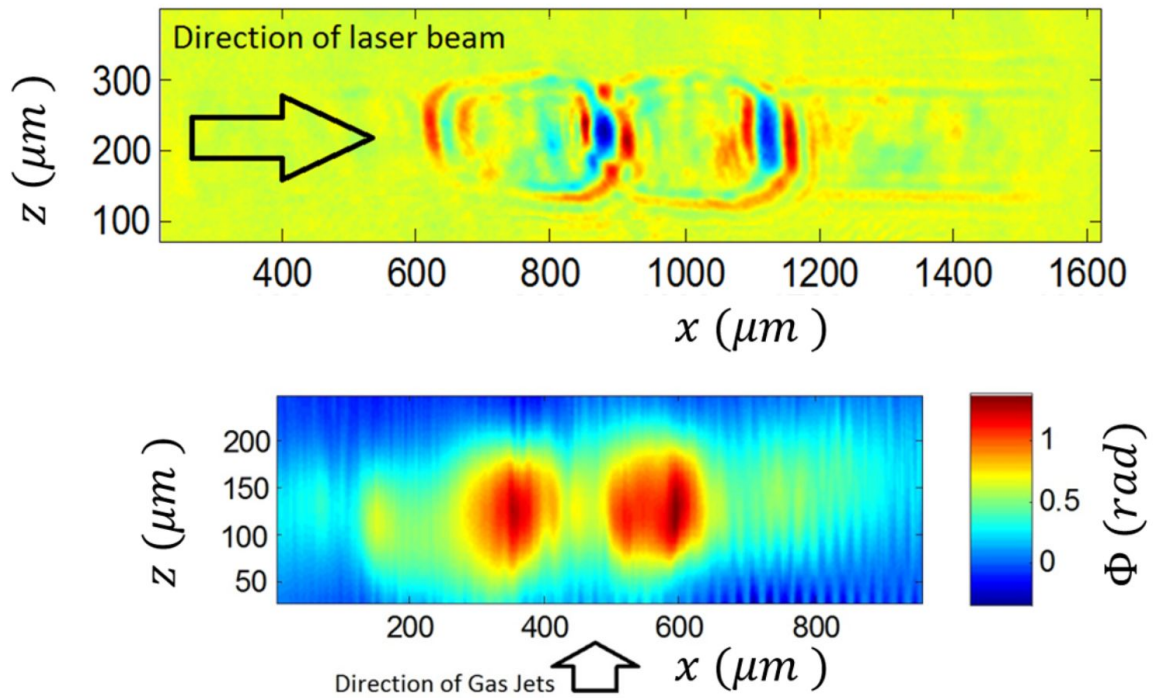
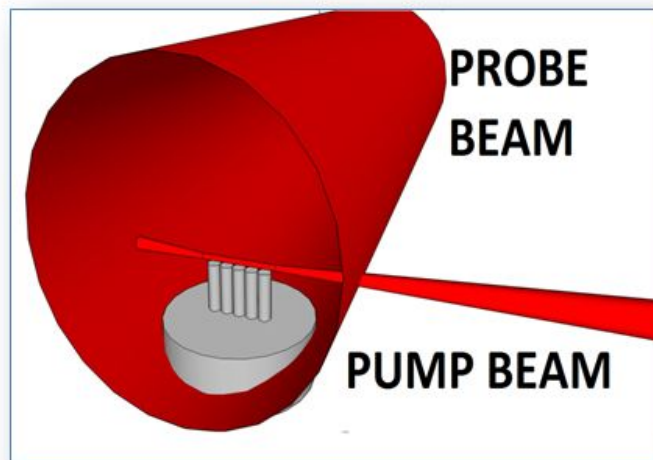


Figure 3.8: Schematic of the femtosecond pump and probe beams to image the shadowgram and interferogram of a corrugated plasma channel produced in the multi-jet array gas jet in continuous flow with  $\sim 30$  fs, 800 nm, 10 mJ laser pulses at 1 kHz repetition rate.

## Chapter 1 References

- [1] Chen, G. *et al.* Ar plasma waveguide produced by a low-intensity femtosecond laser. *Optics Communications* **285**, 2627–2631 (2012).
- [2] Kim, K. Y., Alexeev, I., Parra, E. and Milchberg, H. M. Time-Resolved Explosion of Intense-Laser-Heated Clusters. *Physical Review Letters* **90**, (2003).
- [3] Prencipe, I. *et al.* Targets for high repetition rate laser facilities: needs, challenges and perspectives. *High Power Laser Science and Engineering* **5**, (2017).
- [4] Chen, F., Allou, A., Douasbin, Q., Selle, L. and Parisse, J. Influence of straight nozzle geometry on the supersonic under-expanded gas jets. *Nuclear Engineering and Design* **339**, 92–104 (2018).
- [5] Wieser, M. E. and Berglund, M. Atomic weights of the elements 2007 (IUPAC Technical Report). *Pure and Applied Chemistry* **81**, 2131–2156 (2009).
- [6] Wolterink, T.A.W., High-gradient gas-jet targets for laser wakefield acceleration. *University of Twente*, Master of Science thesis (2011).
- [7] Schmid, K. and Veisz, L. Supersonic gas jets for laser-plasma experiments. *Review of Scientific Instruments* **83**, 053304 (2012).
- [8] Tajima, T. and Dawson, J. M. Laser Electron Accelerator. *Physical Review Letters* **43**, 267–270 (1979).

## Chapter 2 References

- [9] Tomkus, V. *et al.* High-density gas capillary nozzles manufactured by hybrid 3D laser machining technique from fused silica. *Optics Express* **26**, 27965 (2018).
- [10] Jolly, S. W. *et al.* Stereolithography based method of creating custom gas density profile targets for high intensity laser-plasma experiments. *Review of Scientific Instruments* **83**, 073503 (2012).
- [11] Hof, L. and Ziki, J. A. Micro-Hole Drilling on Glass Substrates—A Review. *Micromachines* **8**, 53 (2017).
- [12] Gupta, K. C., Jha, N., Deb, P., Mishra, D. R. and Fuloria, J. K. Determining the mean size and density of clusters, formed in supersonic jets, by Rayleigh scattering and Mach-Zehnder interferometer. *Journal of Applied Physics* **118**, 114308 (2015).
- [13] Salehi, F. *et al.* MeV electron acceleration at 1 kHz with <10 mJ laser pulses: erratum. *Optics Letters* **43**, 1610 (2018).
- [14] Takeda, M., Ina, H. and Kobayashi, S. Fourier-transform method of fringe-pattern analysis for computer-based topography and interferometry. *Journal of the Optical Society of America* **72**, 156 (1982).
- [15] Parra, E., Mcnaught, S. J. and Milchberg, H. M. Characterization of a cryogenic, high-pressure gas jet operated in the droplet regime. *Review of Scientific Instruments* **73**, 468–475 (2002).

- [16] Pretzler, G. A New Method for Numerical Abel-Inversion. *Zeitschrift für Naturforschung A* **46**, (1991).
- [17] Becker, E. W., Bier, K. and Henkes, W. Strahlen aus kondensierten Atomen und Molekeln im Hochvakuum. *Zeitschrift für Physik* **146**, 333–338 (1956).
- [18] Boldarev, A. S., Gasilov, V. A., Faenov, A. Y., Fukuda, Y. and Yamakawa, K. Gas-cluster targets for femtosecond laser interaction: Modeling and optimization. *Review of Scientific Instruments* **77**, 083112 (2006).
- [19] Park, H. *et al.* Size-Dependent High-order Harmonic Generation in Rare-Gas Clusters. *Physical Review Letters* **113**, (2014).
- [20] Hagena, O. F. Condensation in free jets: Comparison of rare gases and metals. *Zeitschrift für Physik D Atoms, Molecules and Clusters* **4**, 291–299 (1987).
- [21] Kim, K. Y., Kumarappan, V. and Milchberg, H. M. Measurement of the average size and density of clusters in a gas jet. *Applied Physics Letters* **83**, 3210–3212 (2003).
- [22] Jang, D. G., You, Y. S., Milchberg, H. M., Suk, H. and Kim, K. Y. All-optical characterization of cryogenically cooled argon clusters in continuous gas jets. *Applied Physics Letters* **105**, 021906 (2014).

### Chapter 3 References

- [23] Rodríguez F., Dorrío B. V., Doval, A. F., Wetter, N. U. and Frejlich, J. Phase difference map interpretation of Mach diamond interferometric patterns by Fourier Transform Methods. *AIP Conference Proceedings* (2008).

- [24] Franquet, E., Perrier, V., Gibout, S. and Bruel, P. Free underexpanded jets in a quiescent medium: A review. *Progress in Aerospace Sciences* **77**, 25–53 (2015).
- [25] Peth, C. *et al.* XUV laser-plasma source based on solid Ar filament. *Review of Scientific Instruments* **78**, 103509 (2007).
- [26] Pirri, A., Corsi, C. and Bellini, M. Enhancing the yield of high-order harmonics with an array of gas jets. *Physical Review A* **78**, (2008).
- [27] Willner, A. *et al.* Coherent Control of High Harmonic Generation via Dual-Gas Multijet Arrays. *Physical Review Letters* **107**, (2011).
- [28] Layer, B., York, A., Varma, S., Chen, Y. and Milchberg, H. Periodic Index-Modulated Plasma Waveguide. *Conference on Lasers and Electro-Optics/International Quantum Electronics Conference* (2009).
- [29] York, A. G., Milchberg, H. M., Palastro, J. P. & Antonsen, T. M. Direct Acceleration of Electrons in a Corrugated Plasma Waveguide. *Physical Review Letters* **100**, (2008).
- [30] Wachulak, P., Bartnik, A., Jarocki, R. and Fiedorowicz, H. Characterization of multi-jet gas puff targets for high-order harmonic generation using EUV shadowgraphy. *Nuclear Instruments and Methods in Physics Research Section B: Beam Interactions with Materials and Atoms* **285**, 102–106 (2012).
- [31] Goers, A. J. *et al.* Multi-MeV Electron Acceleration by Subterawatt Laser Pulses. *Physical Review Letters* **115**, (2015).